

A review of microelectromechanical systems for nanoscale mechanical characterization

This content has been downloaded from IOPscience. Please scroll down to see the full text.

2015 J. Micromech. Microeng. 25 093001

(<http://iopscience.iop.org/0960-1317/25/9/093001>)

View [the table of contents for this issue](#), or go to the [journal homepage](#) for more

Download details:

IP Address: 152.14.136.96

This content was downloaded on 21/08/2015 at 01:18

Please note that [terms and conditions apply](#).

Topical Review

A review of microelectromechanical systems for nanoscale mechanical characterization

Yong Zhu and Tzu-Hsuan Chang

Department of Mechanical and Aerospace Engineering, North Carolina State University Raleigh, NC 27695-7910, USA

E-mail: yong_zhu@ncsu.edu

Received 6 January 2015, revised 24 April 2015

Accepted for publication 27 April 2015

Published 19 August 2015



Abstract

A plethora of nanostructures with outstanding properties have emerged over the past decades. Measuring their mechanical properties and understanding their deformation mechanisms is of paramount importance for many of their device applications. To address this need innovative experimental techniques have been developed, among which a promising one is based upon microelectromechanical systems (MEMS). This article reviews the recent advances in MEMS platforms for the mechanical characterization of one-dimensional (1D) nanostructures over the past decade. A large number of MEMS platforms and related nanomechanics studies are presented to demonstrate the unprecedented capabilities of MEMS for nanoscale mechanical characterization. Focusing on key design considerations, this article aims to provide useful guidelines for developing MEMS platforms. Finally, some of the challenges and future directions in the area of MEMS-enabled nanomechanical characterization are discussed.

Keywords: microelectromechanical system, nanomechanics, nanostructure, nanowire

(Some figures may appear in colour only in the online journal)

1. Introduction

Recent advances in nanotechnology have brought forth a host of nanostructures, such as nanoparticles, nanowires (NWs), nanotubes and graphene, that exhibit ultrahigh mechanical strength (e.g. sample-wide stress $>1/10$ of their ideal strengths) [1]. Such nanostructures are important building blocks for a broad spectrum of nanotechnology applications including energy harvesting and storage [2–4], nanoelectromechanical systems (NEMS) [5, 6], flexible electronics [7, 8] and stretchable electronics [9–11], where ultrahigh strength is of direct relevance. It is known that electronic band gaps change with elastic strain, so do phononic band gaps, thermal transport and other physical and chemical properties. Therefore, ultrahigh strength offers unprecedented opportunities to tune the functional properties of nanostructures through elastic strain

engineering [1]. As an example, Si NWs were found to exhibit an enormous range of elastic strain (e.g. $>12\%$) [12], which is promising for elastic strain engineering.

In addition to the important technological applications, ultra-strength materials provide an excellent platform to study fundamental mechanical behavior at the nanoscale. It is known that size dependent mechanical properties and deformation mechanisms arise as the characteristic dimension of single-crystalline nanostructures approaches 100 nm or so [13, 14]. This has greatly motivated the mechanics of the materials community to investigate nanoscale mechanical behavior from both computational and experimental perspectives. Indeed, the recent rapid advance in nanoscale manipulation/mechanical testing [15, 16] and *in situ* characterization tools such as electron microscopies [17, 18] has enabled real-time observation of deformation and defect dynamics. As the number of

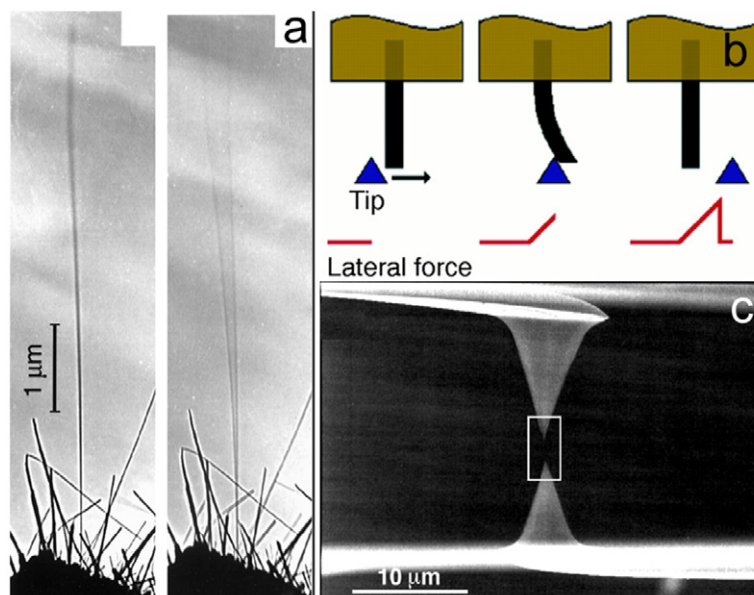


Figure 1. (a) Resonance of a nanotube in response to an electrostatic field in TEM. Reprinted with permission from [19]. Copyright 1999, AAAS. (b) A nanotube deflected by an AFM in the lateral force mode. Reprinted with permission from [24]. Copyright 1997, AAAS. (c) A nanotube mounted between two opposing AFM tips and stretched uniaxially in SEM. Reprinted with permission from [30]. Copyright 2000, AAAS.

atoms in these nanostructures comes increasingly within the reach of state-of-the-art computational modeling capabilities, direct comparison between nano-mechanical tests and atomistic simulations side by side has become closer to reality and holds great promise for important new discoveries in materials science.

Characterizing mechanical properties of individual one-dimensional (1D) nanostructures, the focus of this review is still challenging because of the following requirements: (1) constructing appropriate tools to manipulate, position and align specimens, (2) applying and measuring forces with nano-Newton resolution, and (3) measuring local deformation with nanometer resolution. Existing experimental methods for the mechanical characterization of 1D nanostructures include vibration/resonance in scanning or transmission electron microscopes (SEM or TEM) [19–23], bending using an atomic force microscope (AFM) in different operation modes [24–29], tension/bending/buckling in an SEM with the aid of a nanomanipulator [30–35] (figure 1) as well as nanoindentation [36, 37]. Among all these methods tensile testing is the most straightforward one and it can measure a full spectrum of mechanical properties such as elasticity, plasticity and fracture.

However, the above *in situ* SEM tensile testing systems make it difficult to capture the effect of loading rate and not possible to capture the effects of temperature and environment. A reliable, multifunctional tensile testing apparatus becomes necessitated in order to further understand the mechanical behaviors of 1D nanostructures. MEMS consist of micrometer scale components but they offer nanometer displacement and nano-Newton force resolutions. MEMS actuators and sensors can be integrated on a chip [38]. As such, MEMS have been employed in various nanotechnology-related applications ranging from nanomanufacturing [39] to cell

manipulation [40]. Similarly, MEMS could have the potential to impact nanomechanical characterization through controlled actuation, high-resolution force/displacement measurements, integrated multi-functions and tiny size for *in situ* electron microscopy testing. Zhu and Espinosa have developed an integrated nanoscale testing system using MEMS technology [41–44]. In the past decade, there has been extensive interest in developing MEMS-based instrumentation for experimental nanomechanics that will be reviewed in this article.

In this review, we summarize the recent advances in the field of mechanical characterization of 1D nanostructures using MEMS platforms. We start with three commonly used device configurations and other design considerations such as actuation and load sensing mechanisms, device fabrication, sample preparation and displacement/strain measurement. In section 3, representative MEMS platforms are reviewed in accordance with device configurations. Such platforms have been used for basic tensile testing, fatigue, thermomechanical testing, multiphysical testing, and true displacement-controlled testing via feedback control. In section 4, we highlight several representative studies enabled by the MEMS platforms to demonstrate the wide range of testing capabilities. Finally, some of the challenges and future directions in the area of MEMS-enabled nanomechanical characterization are discussed.

2. Overview

In this section, we present three common device configurations for tensile testing, along with typical MEMS actuation and sensing methods used in the testing. Next, the available microfabrication methods that can be employed to fabricate the testing platforms are presented, followed with a brief review of the manipulation methods used to mount

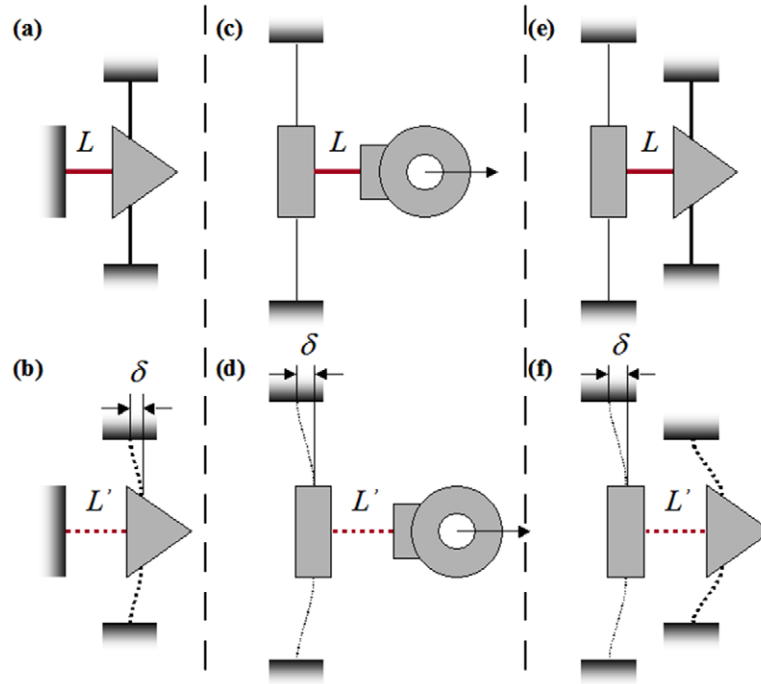


Figure 2. Three typical configurations for uniaxial tension tests. (a, b), (c, d) and (e, f) correspond to the 1st, 2nd and 3rd device configuration defined in section 2.1, respectively. (a, c, e) and (b, d, f) show devices before and after deformation, respectively.

nanostructures onto the MEMS devices and available methods for displacement and strain measurement. In this review, we limit the scope to uniaxial tensile testing, although MEMS devices can be readily applied for compression [44] and bending [45] testing too.

2.1. Device configurations

Tensile test is the most unambiguous testing method to measure mechanical properties. For bulk materials a number of testing machines are commercially available such as those from MTS and Instron. The testing machines typically consist of three parts: a servohydraulic (MTS) or screw-driven (Instron) actuator, a load cell (sensor), and a pair of grips. The same concept prevails at the small scale. There have been considerable efforts in developing instrumentation for micro/nano-scale tensile testing. However, the methods for actuation, sensing and even sample gripping are much different from the large-scale ones. Here we outline three typical device configurations for tensile testing: (1) without a direct load sensor, (2) with a direct load sensor and an external actuator, and (3) with a direct load sensor and an on-chip actuator, which comprises a complete material testing system.

Figures 2(a) and (b) show a schematic of the first device configuration without a direct load sensor. The arrow represents an actuator (e.g. a comb drive actuator or a compliant thermal actuator). A specimen is positioned between the actuator and a fixed post. Before the specimen is positioned (or after it is failed), the actuator displacement δ_0 is recorded as a function of the applied voltage. During the testing, another set of displacement δ ($=L' - L$), which should be smaller than δ_0 due to the finite stiffness of the specimen, is recorded as a function of the same applied voltage. Both specimen displacement

(elongation) and load (thus strain and stress) can be measured based on δ and δ_0 that can be obtained from images or other methods—the elongation is equal to δ , while the load can be calculated based on δ and δ_0 provided the stiffness (or spring constant) K_A of the actuator is known, i.e. $F = K_A \times (\delta_0 - \delta)$. A similar concept has been used in nanoindenters that, of course, operate under compression. For example, a constant load is generated by a magnetic coil under a constant applied voltage no matter how much the nanoindenter travels. Without a substrate, there is an indenter displacement at this constant load. With a substrate, the indenter displacement reduces. In both cases the indenter displacement is recorded by a capacitive sensor or an optical sensor similar to the case of AFM. The load is equal to the displacement difference multiplied by the stiffness of the actuator. Indeed, a nanoindenter has been used in conjunction with a MEMS structure for nanomechanical testing, as will be discussed later. A comb drive actuator is very similar to the nanoindenter, in that they both provide a constant load.

Figures 2(c) and (d) show the second device configuration with a direct load sensor and an external actuator. The device consists of a load sensor supported by spring leafs and a gripping pad. An external actuator can be either hooked [46] or glued [47] to the gripping pad to impose the displacement, while a specimen is positioned between the load sensor and the gripping pad. The load applied on the specimen is equal to that on the load sensor; i.e. $F = K_S \times \delta$, where K_S is the stiffness of the load sensor and δ is the load sensor displacement.

Figures 2(e) and (f) show the third device configuration that consists of both an on-chip load sensor and actuator. The load and displacement of the specimen are measured similar to those discussed for the second device configuration. The major difference is involvement of an on-chip actuator—both

comb drive actuators [43, 48] and thermal actuators [41] have been used. Generally speaking, comb drive actuators can provide a force-control loading condition while thermal actuators provide displacement control assuming the comb drive has low stiffness while the thermal actuator has large stiffness. Displacement control and force control are the two common options available for large-scale machines.

For the first configuration, the advantages include: 1) a simple structure and 2) that one end of the specimen is fixed, which eliminates the rigid body motion due to the sensor displacement and could be helpful for *in situ* observation. The main limitation is that it does not provide real-time load measurement and always requires calibration of the actuator without specimens. For the second configuration, the device structure is also simple. A major advantage is that the external actuators (e.g. piezo-actuators) are commercially available. However, the limitations include a tedious assembly process and the possible misalignment in both in-plane and out-of-plane directions. Although innovative gripping methods have been devised to improve the in-plane alignment [49], out-of-plane alignment is still challenging. The third configuration represents a complete testing system, analogous to large-scale material testing systems. While reduced, misalignment issues could still exist. For instance, residual stress/stress gradient in the MEMS structures could cause out-of-plane deformation leading to an uneven height between the actuator and the load sensor, especially in thin MEMS structures (e.g. those involving polysilicon films), see figure 7 in [44] as an example. In addition, misalignment of the specimens from the axial direction often occurs, which is not a significant concern for NWs or nanotubes when the misalignment is small (e.g. 5° misalignment caused $<1\%$ error in Young's modulus of Pd NWs [42]) but could be for low aspect-ratio specimens [50]. For the third configuration, the system can be fully addressed electronically, which offers an unprecedented opportunity for *in situ* mechanical testing [42]. Besides, the electronic load sensor must be calibrated accurately, which might not be trivial.

2.2. MEMS actuators and sensors

A number of actuation mechanisms have been implemented in MEMS including electrostatic actuation, thermal actuation, piezoelectric actuation, and shape memory alloy actuation [51, 52], among which the former two have been widely used for MEMS-based mechanical testing due to their compatibility with conventional microfabrication techniques.

An electrostatic actuator is based on the attraction of two oppositely charged plates. In particular, a comb drive type electrostatic actuator makes use of a large number of interdigitated 'fingers' that are actuated by applying a voltage between them [53, 54] (figure 3(a)). A comb drive actuator can generate a relatively large travel range ($\sim 10\mu\text{m}$ or more). A distinctive feature of the comb drive actuator is that the electrostatic force is nearly constant over the travel range at a given voltage. The comb drive actuator has been widely used in the MEMS field. However, as an actuator an undesirable feature for mechanical testing is that it requires a large

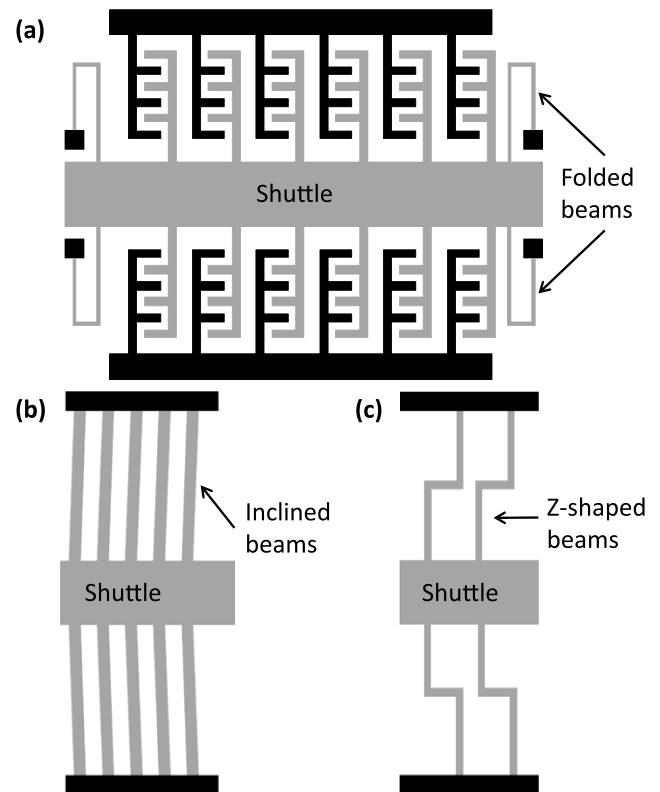


Figure 3. Schematics of common in-plane mechanical actuators. (a) Comb drive actuator, (b) V-shaped thermal actuator, (c) Z-shaped thermal actuator. The black and grey colors represent anchors and moveable parts, respectively.

actuation voltage (often $>50\text{V}$), which might cause instability (pull-in) of the comb structure.

A thermal actuator relies on thermal expansion of the structural materials. Thermal actuators in a variety of configurations have been exploited for achieving in-plane motion, including U-shaped [55], V-shaped [41, 56] and Z-shaped actuators [57, 58]. For these actuators, when an electric current passes across the freestanding beams, Joule heating results in thermal expansion, leading to linear forward motion in the cases of V-shaped (figure 3(b)) and Z-shaped (figure 3(c)) actuators. A V-shaped actuator is very stiff and can provide a quite large force ($\sim 10\text{mN}$) at a relatively low actuation voltage, while a Z-shaped actuator is much more compliant and could be used simultaneously as a sensor. Both types of thermal actuators are typically limited in terms of travel range ($\sim 1\text{--}2\mu\text{m}$). A critical challenge for using thermal actuators in nanomechanical testing is the undesired heating of the specimen. To mitigate this problem, Zhu *et al* introduced heat sink structures to dissipate heat and hence decrease the temperature rise at the specimen region to below 5°C [41, 59], without adding complexity in the fabrication process (e.g. extra steps to introduce a heat isolation structure between the actuator and the specimen). In vacuum the more heat sink beams between the thermal actuator and the specimen, the more heat dissipation there is [41, 59]. In air a larger distance between the actuator and the specimen also helps (even without the heat sink beams) due to the heat dissipation to the air [60]. Abbas *et al* designed a cascaded thermal

actuator that was able to provide $>10\mu\text{m}$ displacement (at reduced stiffness) while the temperature near the specimen could remain as low as 50°C [61].

A load sensor typically consists of a flexible member, so the load is measured as the sensor displacement multiplied by the sensor stiffness. Displacement sensing mechanisms commonly used in MEMS include capacitive sensing, piezoresistive sensing, piezoelectric sensing and tunneling sensing [51, 52]; the former two have been used for MEMS-based mechanical testing, again due to their compatibility with conventional microfabrication techniques.

Capacitive sensing is perhaps the most popular sensing mechanism in MEMS with commercial chips available for data acquisition. In principle any structure consisting of two plates separated by a gap is a capacitor. It is very difficult to measure the absolute capacitance in MEMS and the capacitance change does not readily correlate with the sensor displacement due to the presence of parasitic capacitances and stray capacitances. So typically a differential capacitive sensor is used in a MEMS testing platform. Capacitive sensors are typically insensitive to temperature. For these reasons, differential capacitive sensors have been widely used in many MEMS devices such as accelerometers [61]. Parasitic capacitances can be mitigated by a commercially available sensing module (MS3110, MicroSensors) [42, 63, 64]. In addition, it is suggested that the MEMS package is placed as close as possible to the sensing module in order to diminish stray capacitance and electromagnetic interference [42].

The piezoresistive effect is a change in the electric resistivity of a semiconductor when mechanical strain is applied. The gauge factor (the ratio between relative resistance change and strain) can be as large as 200 for diffused semiconductors. Si is a common piezoresistive material including single-crystalline and polycrystalline Si, therefore piezoresistive sensing is widely used in MEMS devices [65]. Piezoresistive sensors are typically sensitive to temperature, although methods like the Wheatstone bridge can be used to cancel out the temperature effect.

2.3. Fabrication

In general, silicon-based microfabrication methods include surface micromachining and bulk micromachining [51]. Surface micromachining is based on the deposition and etching of different structural layers on top of the substrate. To obtain freestanding structures, sacrificial layers that can be etched later to release the structural layers are required. By contrast, in bulk micromachining a Si substrate (wafer) is selectively etched to produce freestanding structures. Usually the structure thickness is a few micrometers in surface micromachining, and tens to hundreds of micrometers in bulk micromachining. A special bulk micromachining method involves silicon-on-insulator (SOI) wafers, where an insulator layer (i.e. silicon dioxide) is embedded between a structural layer of single-crystalline Si (with thicknesses ranging from submicrometer to $50\mu\text{m}$) and a Si substrate.

To design a MEMS testing platform, two important factors should be considered: system stability, and load sensor

sensitivity. The in-plane bending stiffness of the actuator should be large compared to the specimen stiffness in order to keep the system stable. The out-of-plane bending stiffness of the entire device should be large to prevent out-of-plane deformation as well as possible stiction (adhesion) to the substrate. For these reasons a relatively large device thickness is preferred if possible. On the other hand, a small in-plane bending stiffness of the load sensor is desired to achieve a high load resolution, which could be achieved by tuning the width of the sensing beams.

A number of customized fabrication processes have been developed to fabricate MEMS testing platforms. Saif and McDonald used a single crystal silicon reactive etching and metallization (SCREAM) process to fabricate a large-scale comb drive actuator that can generate force in the order of a milli-Newton [66]. Deep reactive ion etching (DRIE) of a Si substrate was used to create structures as deep as $12\mu\text{m}$. Haque and Saif developed a process that combines both surface micromachining and bulk micromachining to fabricate a platform including a $100\mu\text{m}$ thick device structure and a 100nm thick freestanding aluminum film [49]. Corigliano *et al* used a thick epipoly layer for microactuators and accelerometers (ThELMA) process developed at STMicroelectronics to fabricate a platform including a comb drive actuator [67] or thermal actuator [68] (with a thickness of $15\mu\text{m}$) to test polycrystalline Si specimens. Lu *et al* used Si ($130\mu\text{m}$ thick) on a glass substrate made by wafer bonding to achieve a device with large out-of-plane rigidity [69]. Naraghi *et al* fabricated a MEMS platform [47, 70] using surface micromachining following a process previously developed by Kahn *et al* [54]. The device layer was made of polycrystalline Si with a thickness of $5.2\mu\text{m}$. Kiuchi *et al* developed a comb drive based platform using a SOI wafer with a $35\mu\text{m}$ thick Si device layer, including patterning of the Si layer to define the device and backside etching [71]. A number of MEMS platforms have been fabricated using similar SOI processes [61, 64, 72–75]. Of special note is that Zhang *et al* [76] fabricated a MEMS platform also using a SOI wafer, but with a patterned SiO_2 insulator layer beneath the structural layer, in order to achieve electrical isolation between the sample area and the actuator and the load sensor.

Commercially available MEMS fabrication processes have been used to fabricate MEMS testing platforms. Two well-known processes are multi-user MEMS processes (MUMPs) at MEMSCAP (Durham, NC) and Sandia ultra-planar, multi-level MEMS technology (SUMMiT) at Sandia National Labs. These processes typically involve multiple structural layers that offer design flexibility to the users. MEMSCAP offers three types of processes that could be used to fabricate MEMS testing platforms, Poly-MUMPs, SOI-MUMPs and MUMPs-PLUS. Poly-MUMPs provides two structural layers of polycrystalline Si (2 and $1.5\mu\text{m}$ thick, respectively) using surface micromachining [43, 77]. SOI-MUMPs provides one structural layer (10 or $25\mu\text{m}$ thick) using the SOI technology [61, 78, 79]. Zhu and Espinosa collaborated with MEMSCAP to develop the first MUMPs-PLUS process based on Poly-MUMPs, where a backside window required for *in situ* TEM was made possible [42, 44]. The MUMPs-PLUS process based on SOI-MUMPs

was recently developed to keep part of the silicon oxide layer beneath the structural Si layer, which can serve as electrical isolation between the structures [80]. de Boer and co-workers used the SUMMiT process to fabricate MEMS platforms [81–83]. These commercial processes produce MEMS devices with high yield, reproducibility, and design flexibility, significantly facilitating the advance of the field.

2.4. Sample preparation

A key step in nanoscale mechanical testing is to position specimens at desired locations with nanometer resolution and high throughput. For tensile testing, this step becomes even more challenging compared to other types of testing methods as the specimens must be freestanding, aligned with the loading direction, and clamped at both ends. Methods for the manipulation and positioning of nanostructures onto MEMS devices mainly include ‘pick-and-place’ by nano-manipulation [42] and dielectrophoresis [84, 85] in addition to co-fabrication and direct synthesis. Here we briefly discuss these sample preparation methods, while more details can be found elsewhere [15, 86].

A widely used method for mounting nanostructures onto MEMS devices is ‘pick-and-place’ by nanomanipulation, introduced by Zhu and Espinosa [42]. In this method, a nanomanipulator is employed to pick and transfer a desired sample from the substrate to a target location inside a SEM or a dual-beam (SEM/FIB). Electron beam induced deposition (EBID) of residual hydrocarbon in a SEM chamber or a precursor gas (e.g. platinum), is commonly used for clamping the samples. This method has been used successfully for a wide range of nano-structures [12, 76, 87–91]. Admittedly this method is tedious. The carbon- or platinum-containing materials could form amorphous contamination on the sample surface. There is also concern about whether the clamping mechanism is sufficiently rigid and reproducible. Gianola and co-workers recently reported artifacts in the strain measurement directly between the clamps due to compliance and permanent deformation of the clamps [92]. Zhu and co-workers also found the measured Young’s modulus of a NW (using the resonance method) depends on the clamping. But they pointed out that the true Young’s modulus can be measured if the critical clamp size is reached. The critical clamp size is a function of the NW diameter and modulus ratio of the clamp material and the NW. Note that their work was for resonance (or bending). Further investigation on the effect of clamping on mechanical behavior measured under tension is warranted. Meanwhile, displacement markers deposited along the NW length have been used for local displacement measurement [91–93]. To alleviate the issues of EBID, adhesives (e.g. epoxy) have been used to clamp polymer nanofibers [70], CNTs [94] and Au nanobeams [95]. With adhesives, manipulating an individual specimen can only be done in air under an optical microscope, which might limit this method to relatively large specimen sizes. Compliance of the adhesives could also be of potential concern.

Dielectrophoresis has been used to mount CNTs [84] and GaN NWs [85] onto MEMS devices. While this method is

more scalable than the ‘pick-and-place’ one, the yield is typically low and contamination during the process is quite common.

Directed synthesis is a promising method that could potentially eliminate the issues with the ‘pick-and-place’ approach. The boundary conditions are supposed to be robust. Mass production that avoids the tedious manipulation process could be possible. However, so far only limited materials have been synthesized, including Si NWs [96] and Ge NWs [97] between microfabricated Si posts. In addition, no direct synthesis into movable MEMS devices has been reported. Co-fabrication is another method, while the materials that can be co-fabricated are typically limited. C₆₀ NWs [74], Au NWs [75], and Pt ultra-thin films [61] have been successfully co-fabricated with MEMS devices for *in situ* tensile testing.

2.5. Displacement/strain measurement

Accurate and non-contact displacement/strain measurement is critical in the mechanical testing of nanostructures. The simplest method is to compare images of two markers on the specimen before and after the deformation. For 1D nanostructures, the markers can be made by EBID of carbon or platinum on the specimen surface [93]. The gap between the actuator and the load sensor can also be used to measure specimen displacement without the local markers, provided that there is no sliding between the specimen and the MEMS device. Since nanomechanical testing is typically conducted inside SEM or TEM, high-resolution images of the specimen can be readily obtained. The displacement resolution can be as high as half a pixel.

The manual operation of image correlation, however, can be tedious. In order to increase the yield as well as improve the resolution, a digital image correlation (DIC) algorithm can be used. DIC is a method based on comparing images of an area with random features on the specimen before and after the deformation. This method has been widely used for measuring displacement/strain using optical images [98–100] and recently extended to SEM images [101–103]. Correction schemes have been developed to account for issues like spatial distortion, time-varying distortion (drift distortion) and random step changes (image shift) in SEM images. In addition, a high beam current and long dwell time were recommended to minimize inherent noise of the electron beam [104]. The recommendations might extend from the microscale to the nanoscale with the caution that a high electron beam could introduce radiation damage to nanostructures.

Naraghi *et al* obtained the specimen displacement and strain by measuring the displacements of the MEMS structures (not directly of the specimen) using DIC of optical images [105]. FIB milling was used to introduce the random features on the otherwise smooth surface of the MEMS structures. Yilmaz and Kysar used the same DIC method but with SEM images [75]. Gianola *et al* applied DIC directly on a single NW, where the natural contrast along the length of the NW, presumably from a carbonaceous layer that had formed as a result of SEM imaging, was used as the random features [106]. In this case, DIC can provide displacement/strain information along the

entire NW, which could be useful to indicate if the strain is uniform or there exists localized necks or slip lines. The accuracy of DIC can reach 1/8 of a pixel or better.

Both methods above require a series of images capturing the specimen deformation. For the *in situ* SEM/TEM testing, microscopy imaging at low magnification is needed to obtain the specimen displacement and sometimes the load, which might sacrifice the opportunity to observe deformation mechanisms at high magnification or at least requires switching between the magnifications and related electron beam conditions. The imaging rate is generally low. And it is time-consuming to analyze a large number of images for image correlation. In some other cases, *ex situ* testing is required or *in situ* testing is unnecessary, e.g. to study fatigue behavior under a controlled environment. Therefore, the electronic readout of the displacement/strain without the need of imaging becomes desirable. Espinosa *et al* first developed a MEMS platform with two capacitive sensors [44]; the difference of the displacements measured by the two sensors is the specimen displacement. Pierron and co-workers implemented such a two-sensor scheme to study Ni nanobeams [63] and this was later applied on fatigue behavior study of nanostructures, both *in situ* and *ex situ* [95].

3. MEMS testing platforms

In this section, MEMS testing platforms for basic tensile testing will be reviewed according to the three device configurations aforementioned, followed with those for more advanced testing such as fatigue testing and multiphysical testing. For the basic tensile testing, recent efforts on feedback control of the load sensor in order to achieve true displacement control will be presented. Only a few representative platforms can be discussed in this section, but other platforms are summarized in table 1. While MEMS have been used to test micro- or sub-micro-scale specimens [81, 107], this review is focused on nanoscale specimens. A review on microscale characterization can be found in [108].

3.1. Platforms for basic tensile testing

3.1.1. First configuration. Using the first device configuration, Lu *et al* developed a MEMS platform consisting of a custom-made thermal actuator [69]. The platform was used to test template carbon nanotubes that were mounted onto the platform using dielectrophoresis [109]. Kiuchi *et al* [71] developed a MEMS platform consisting of a comb drive actuator (1000–5000 pairs of combs) using the SOI process. A unique feature of this platform is a cantilever that serves as an amplification system for measuring the tensile displacement of the specimen. The amplification system was able to magnify the actuator displacement by over 90 times. Using optical microscopy, a resolution of 30 nm in the cantilever deflection was acquired, translating to 0.29 nm in the actuator displacement. Carbon NWs directly synthesized on the platform by FIB-assisted chemical vapor deposition using phenanthrene ($C_{14}H_{10}$) were tested. Brown *et al* [77] built a MEMS platform consisting of

a V-shaped thermal actuator using the Poly-MUMPS process. The specimen displacement was measured from SEM images. Loading and unloading behaviors of carbon nanofibers [77] and gallium nitride NWs [85] were measured inside SEM. Both pick-and-place and dielectrophoresis methods were used for mounting the specimens.

Of particular note is the ‘push-to-pull’ concept that has been applied to the MEMS platforms. Such a platform typically involves an existing transducer (e.g. nanoindenter) and a micro-fabricated structure that can convert compression from the transducer to tension on the nanostructure. Hysitron developed a push-to-pull platform that can be used together with their TEM nanoindentation holder to perform *in situ* TEM tensile testing [110]. As shown in figure 4(a), the platform consists of a fixed part and a freestanding part that is supported by four folded beams. While an indenter head pushes the freestanding part from the left-hand side, the gap between the fixed and freestanding parts expands and applies a tensile load to the specimen that is bridged across the gap. Guo *et al* employed this platform to study phase transition of VO_2 NWs by *in situ* TEM [91, 111]. Lu *et al* developed another type of push-to-pull MEMS platform that converts compression from a nano-indenter to tension in the orthogonal direction inside SEM and TEM, as shown in figure 4(b) [112]. This device further developed the concept of the Theta-like specimen [113, 114] that was used for mechanical testing of micro-fabricated small-scale structures. This platform has been used to perform *in situ* SEM and TEM tensile testing of metal NWs [115, 116] and carbon nanotubes [94]. For both push-to-pull platforms, a calibration test on the platform without the specimen is necessary. The load on the specimen is obtained from the nanoindenter readout by comparing the cases with and without the specimen, providing that the structural response (e.g. stiffness) of the platform is known; the specimen elongation is measured by SEM or TEM imaging. For accurate load measurement, the alignment between the nanoindenter and the platform is critical.

3.1.2. Second configuration. Using the second device configuration, Naraghi *et al* have developed a MEMS platform that is actuated by an external piezoelectric actuator [47], see figure 5(a). The platform includes a leaf-spring load sensor, a gripping pad and a gap in between to mount the specimen. A tipless AFM cantilever connects the three-axis piezo-actuator and the gripping pad. Both load and elongation of the specimen were obtained from optical images of the MEMS platform using DIC. As illustrated in figure 5(b), the displacements were measured by tracing rigid-body motions of three different regions in the image—Region 1 represents the device substrate, Region 2 the load sensor, and Region 3 the grip where the AFM cantilever is attached (note here the loading direction is towards the left side). The specimen elongation was recorded as $U_2 - U_3$, while the load on the specimen was equal to the load sensor displacement ($U_2 - U_1$) multiplied by the sensor stiffness. The displacement resolution using this method was 1/8 of a pixel, equivalent to 50 nm or better (from optical images). Electrospun polyacrylonitrile (PAN) nanofibers were tested using this platform.

Table 1. Summary of MEMS platforms for tensile testing of 1D nanostructures.

Device type	Fabrication method	Thickness (μm)	Actuator type	Strain measurement	Load sensing	Tested materials
1st	SOI	35	Electrostatic	Optical image	Optical image with cantilever amplifier (0.3 nm)	Carbon [70]
	Poly-MUMPS	3.5	Thermal Indenter	SEM image (40 nm)	SEM image	Carbon NF [77], GaN [85]
	SOI	5	Indenter	SEM DIC	Nanoindenter readout	VO ₂ [91, 111], MO [157]
	SOI	9.5	Indenter	Nanoindenter readout	Nanoindenter readout	Carbon NT [94], Ni [115], Cu [158]
2nd	LPCVD Poly-Si	5.2	Piezo	Optical DIC (25 nm)	Optical DIC	Polymeric NF [47, 70], carbon NF [159]
	SOI	10	Piezo	SEM image (1 nm)	SEM image	ZnO [119]
3rd	Poly-MUMPS	3.5	Thermal	SEM/TEM image	Capacitance (0.05 fF = 1 nm)	Pd [42], carbon NT [87, 160], ZnO [88, 161], Ag [131], GaN [162]
			Electrostatic			Polymeric NF [105]
	SUMMiT	6	Electrostatic	Optical DIC (20 nm)	Optical DIC	Ni [63, 60], Au [95]
	SOI-MUMPS	10	Thermal	Capacitance	Capacitance (0.05 fF = 0.25 nm)	Pd [89]
	SUMMiT	—	Thermal	SEM DIC (2 nm)	DIC	Co [90], Si [120]
	SOI	100	Electrostatic	SEM image	SEM image (<10 nm)	Si [76]
	SOI	25	Electrostatic	Capacitance	Capacitance (1.5 nm)	Si [78, 156]
	SOI-MUMPS	25	Thermal	SEM image (6 nm)	SEM image	C ₆₀ [74, 163]
	SOI	5	Electrostatic	Capacitance	Capacitance (0.1 fF = 1 nm)	Pt (ultrathin film) [61]
	SOI	20–25	Thermal	Optical DIC (15 nm)	Optical DIC	Au [75]
	SOI	No	Electrostatic	SEM DIC (7.5 nm)	SEM DIC	Si [121], SiC [79], Ag [93]
	SOI-MUMPS	10	Thermal	SEM image (1 nm)	Capacitance	

Note: Displacement resolution, when available, is included after the corresponding strain measurement and/or load sensing. The tested materials are NWs by default. NT: nanotubes; NF: nanofibers.

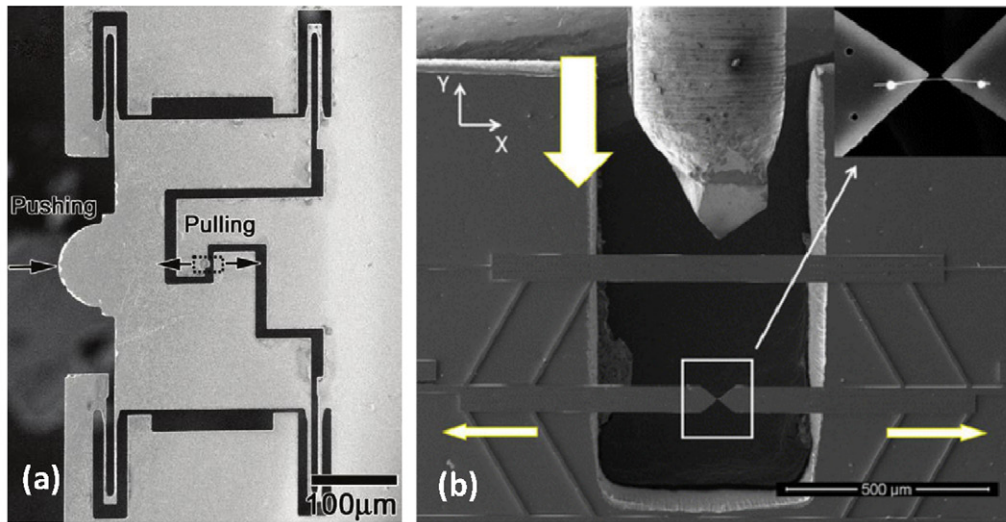


Figure 4. (a) SEM image of the push-to-pull platform by Hysitron for *in situ* TEM testing. A nanointer head pushes the movable part from the left side. Reprinted with permission from [91]. Copyright 2011, American Chemical Society. (b) SEM image of the push-to-pull platform by Lou and co-workers. A nanointer header pushes from the top. Reprinted with permission from [112]. Copyright 2010, Springer.

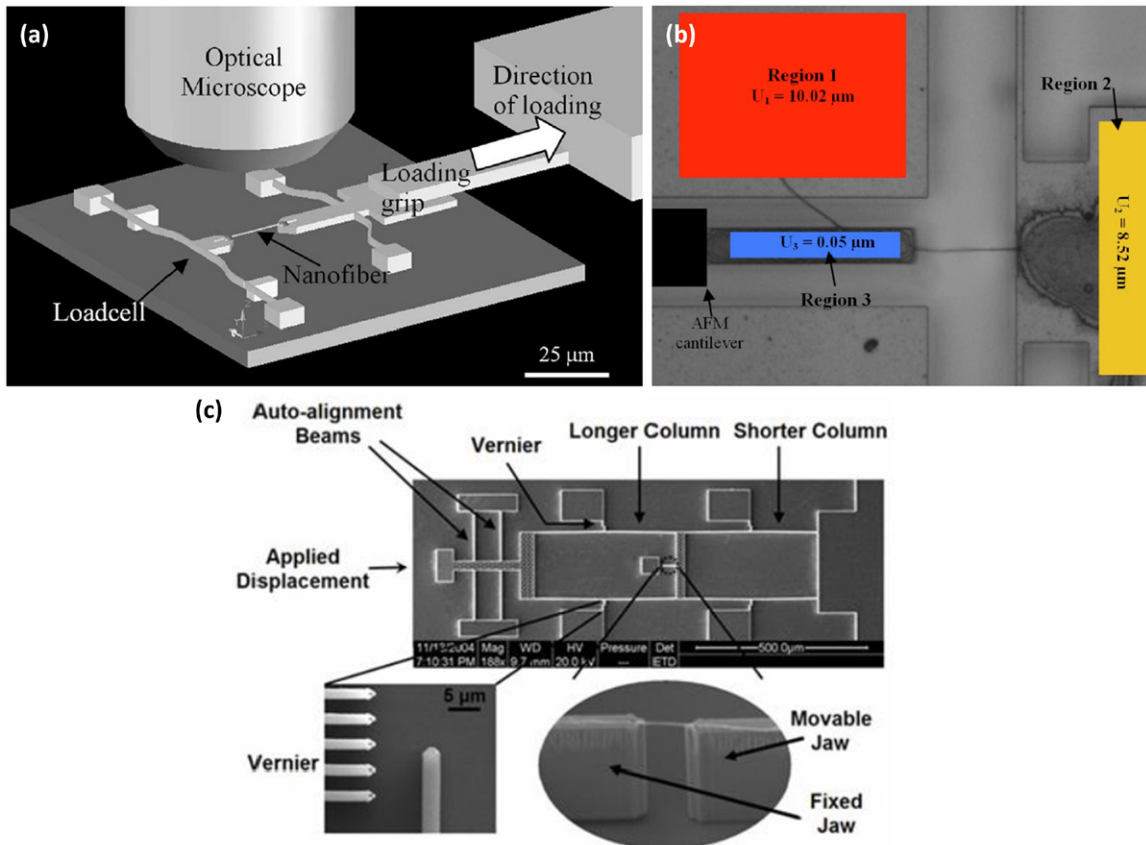


Figure 5. (a) The MEMS platform consisting of a loadcell, actuated by an external actuator for nanofiber testing. (b) DIC displacement measurement. (a) and (b) Reprinted with permission from [70] and [47]. Copyright 2007, AIP Publishing LLC. (c) The push-to-pull MEMS platform by Haque and co-workers. An external piezo-actuator pushes from the left side [119].

Haque and Saif introduced a MEMS platform to characterize nanoscale thin films inside SEM and TEM [49, 117, 118]. The platform was actuated by an external piezo-actuator in the ‘pulling’ direction. A U-shaped structure was co-fabricated in the platform to help mitigate the misalignment between the

actuator and the specimen. Later Desai and Haque developed a platform using the push-to-pull mechanism, with an independent load sensor, to study 1D nanostructures, as shown in figure 5(c). When the platform is pushed by an external piezo-actuator, the specimen across the movable jaw and fixed jaw

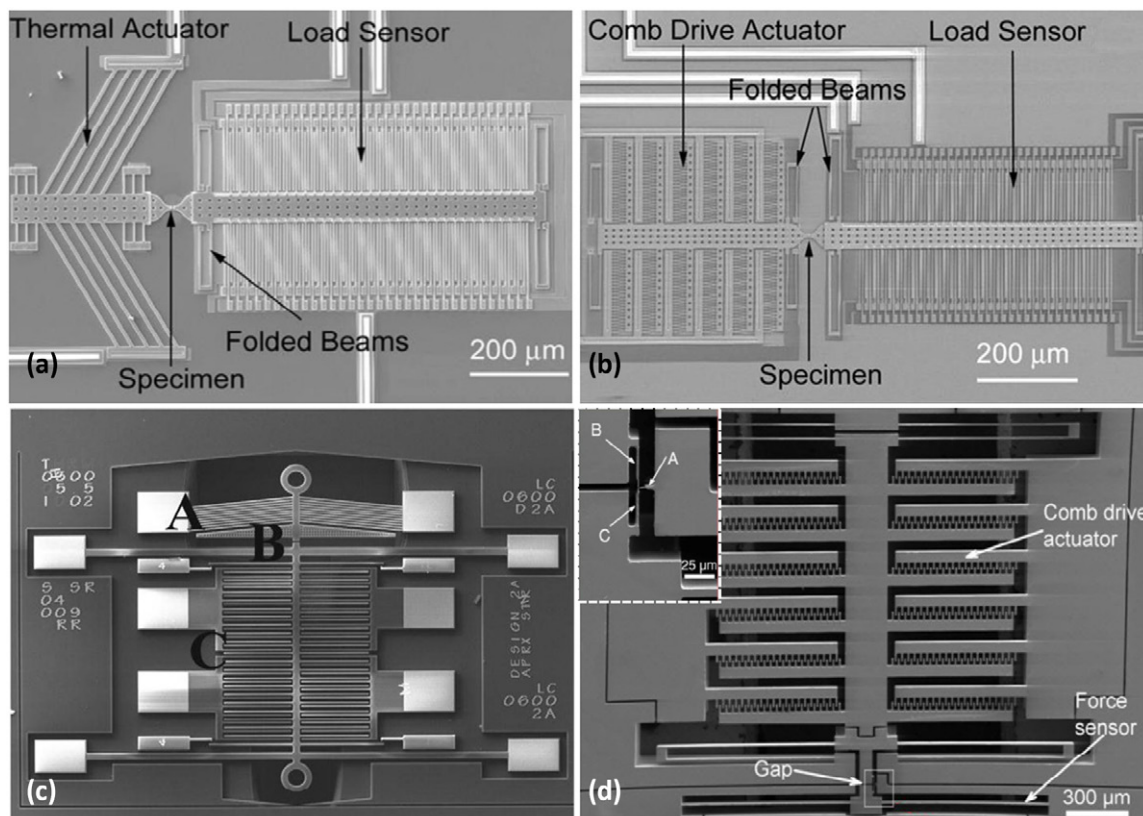


Figure 6. A MEMS platform including a thermal actuator (a) or comb drive actuator (b), a capacitive load sensor and a specimen in between (fabricated by Poly-MUMPs) [43]. (c) A platform consisting of a thermal actuator, a specimen gap, and a capacitive load sensor (fabricated by SOI-MUMPs). Reprinted with permission from [156]. Copyright 2013, AIP Publishing LLC. (d) A platform including a comb drive actuator and a beam load sensor. Reprinted with permission from [90]. Inset shows a magnified view of the three-beam structure, which is attached to the device in the boxed area. Copyright 2009, IOP Publishing.

is stretched. The authors introduced an interesting design that is based on buckling of sensing beams (columns). The load on the specimen is the difference of the forces on the longer columns and shorter columns, while the specimen elongation is also related to the lateral displacement of the buckled beams. The lateral displacement of a sensing beam (1000, 2 and 10 μm in length, width and thickness, respectively), when buckled, is about 40 times larger than the specimen elongation. The large amplification makes it possible for an optical microscope to measure specimen elongation and the load on the specimen. Using this device, ZnO NWs [119] and pyrolysed poly-furfuryl alcohol nanofibers [46] were tested.

3.1.3. Third configuration. Using the third device configuration, Zhu and Espinosa have developed a MEMS platform that includes an on-chip actuator and an electronic load sensor with a gap in between [42]. Two types of MEMS actuators were used, a thermal actuator for displacement control as shown in figure 6(a) and a comb drive actuator for force control as shown in figure 6(b). A major advance in their work was the introduction of a capacitance load sensor that measures displacement electronically, based on differential capacitive sensing rather than microscope imaging. The MEMS platforms were fabricated using Poly-MUMPs and MUMPs-PLUS for the *in situ* SEM and TEM testing, respectively. Since then, a large number of MEMS platforms using

this configuration have been reported. For instance, Cheng *et al* used the same design but fabricated a platform using SOI-MUMPs to study mechanical properties of SiC [79] and Ag NWs [93]. Steighner *et al* fabricated a platform that includes a V-shaped thermal actuator and a capacitive load sensor using SOI-MUMPs, as shown in figure 6(c). The platform has been used for *in situ* SEM tensile testing of Si NWs [78].

Figure 6(d) shows a MEMS platform developed by Zhang *et al*, that consists of a comb drive actuator and a simply folded beam that serves as the load sensor [90]. A three-beam structure, as shown in the inset of figure 6(d), was fabricated near the specimen gap to capture specimen elongation and load sensor displacement in one image. Cobalt [90] and Si NWs [120] were tested using this platform. Chen *et al* has reported a platform that employed a similar structure for the mechanical testing of Pd NWs [89]. The platform consists of a V-shaped thermal actuator, a load sensor comprised of folded beams, and a comb structure adjacent to the sample that is attached to the platform and the substrate (similar to the three-beam structure mentioned above). This platform was developed as part of the Sandia Discovery Platforms.

3.2. Platforms for fatigue testing

Pierron and co-workers have developed a MEMS testing platform that consists of two separated capacitive sensors

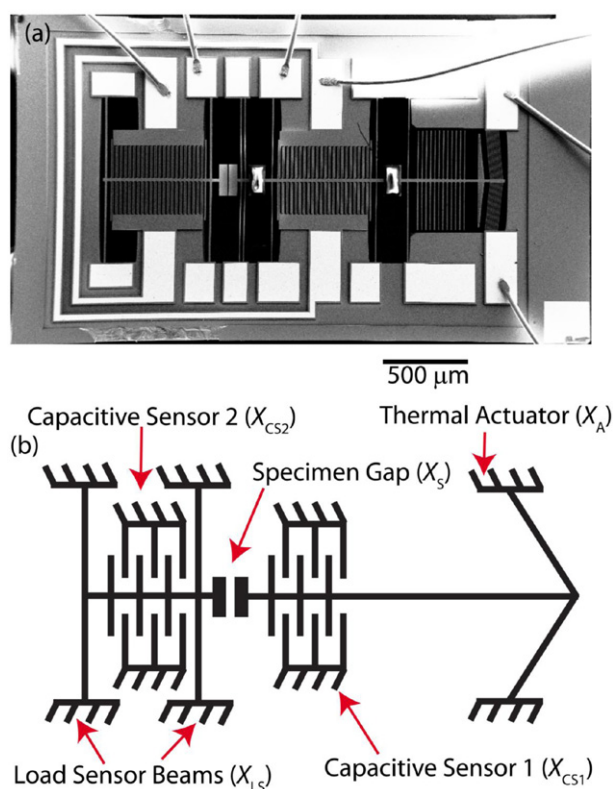


Figure 7. (a) SEM image of a MEMS platform for the fatigue test that consists of a thermal actuator, a nanospecimen gap (NG), and two capacitive sensors (one on each side of the specimen gap). Reprinted with permission from [95]. (b) Corresponding schematic, with a description of its components and their displacements (e.g. X_A : displacement of thermal actuator). Copyright 2013, Royal Society of Chemistry.

to record both the specimen displacement and load [63, 95]. Since high-resolution images are not mandatory for strain measurement in this case, the platform can be used for *ex situ* experiments that can study environmental effects in air as an example. As shown in figure 7, the MEMS platform includes a V-shaped thermal actuator, a heat sink, a specimen gap, and two capacitive sensors (one on each side of the specimen gap). The load can be acquired from the capacitance change in CS2, while the specimen displacement is extracted from the difference between CS1 and CS2. The area circled by the grey rectangles in figure 7 shows the electrical isolation between thermal actuator, and CS1 and CS2 using an electrically insulating epoxy, which avoids electrical interference between the actuator and sensors. The platform has been used to perform fatigue test of Au ultrathin films (nanobeams) [95].

3.3. Platforms for thermomechanical testing

1D nanostructures have been demonstrated as the building blocks of next-generation electronics and sensors. For device applications it is inevitable for nanostructures to experience different temperatures. Thus, it is of relevance to characterize their thermomechanical behavior. Chang and Zhu have recently developed a MEMS thermomechanical platform with an on-chip heater for the *in situ* mechanical testing of

1D nanostructures from room temperature to 600 K [121]. The MEMS platform consists of a comb drive actuator, a capacitive load sensor, a specimen gap, and a heater based on Joule heating in close proximity to the specimen gap, as shown in figure 8(a). The entire platform is symmetric to ensure the same temperature on both sides of the specimen to avoid temperature gradient and heat flow through the specimen; note that the capacitive sensor is also in the form of a comb drive, identical in geometry to the comb drive actuator. A fully 3D multiphysics simulation was used to predict the temperature distribution in both air and vacuum environments. The temperature distribution in air was measured by Raman spectroscopy and agreed well with the simulation result. The heater consists of eight Z-shaped beams, whose dimensions were carefully designed in order to purposely compensate the thermal expansion of the long axial shuttles of the actuator and sensor during heating. The mechanical properties of single-crystalline Si NWs were tested inside a SEM at different temperatures to investigate their BDT behavior [121].

Chen *et al* integrated their MEMS platform inside a vacuum cryostat including a heater, a cooling channel with liquid nitrogen circulation and a PID temperature controller [122]. The vacuum chamber has a fused silica window on top so that the MEMS platform inside can be viewed by an optical microscope. The experimental setup is shown schematically in figure 8(b). Their setup is capable of achieving a temperature range from 77 to 475 K, with the largest 0.035 K min^{-1} drift. Defect-free $\langle 110 \rangle$ Pd NWs were tested to demonstrate the capability of the setup. A temperature dependent stress-strain behavior was found in these Pd NWs.

Kang and Saif developed a novel MEMS platform for *in situ* uniaxial test of micro/nanoscale samples at high temperature [123]. Fabricated out of SiC, this platform was able to sustain temperatures up to 700°C , which is much higher than those made of Si. Based on the design by Haque and Saif earlier [49], a Joule heating mechanism and a local bi-metal type temperature sensor were incorporated for heating and temperature measurement, respectively, as shown in figure 8(c). It is of note that microfabricated heaters have been used in thermomechanical testing platforms for microscale films [124].

3.4. Platforms for multiphysical testing

It is of fundamental and technological importance to understand the multiphysical coupling of nanostructures. Of particular interest to the mechanics community is how mechanical strain can alter other physical properties including charge carrier transport and phonon transport among others—so-called elastic strain engineering. Nanostructures typically exhibit ultrahigh mechanical strength, thus offer unprecedentedly large room for elastic strain engineering. Bernal *et al* developed a MEMS platform using MUMPs-PLUS to characterize electromechanical coupling of NWs, by integrating four-point electric measurement and tensile loading [125]. Based on the original design that consists of a thermal actuator, a specimen gap and a capacity load sensor, four conductive support beams were added to form electrical paths to the interconnects on the device shuttles where the specimen was positioned, as shown

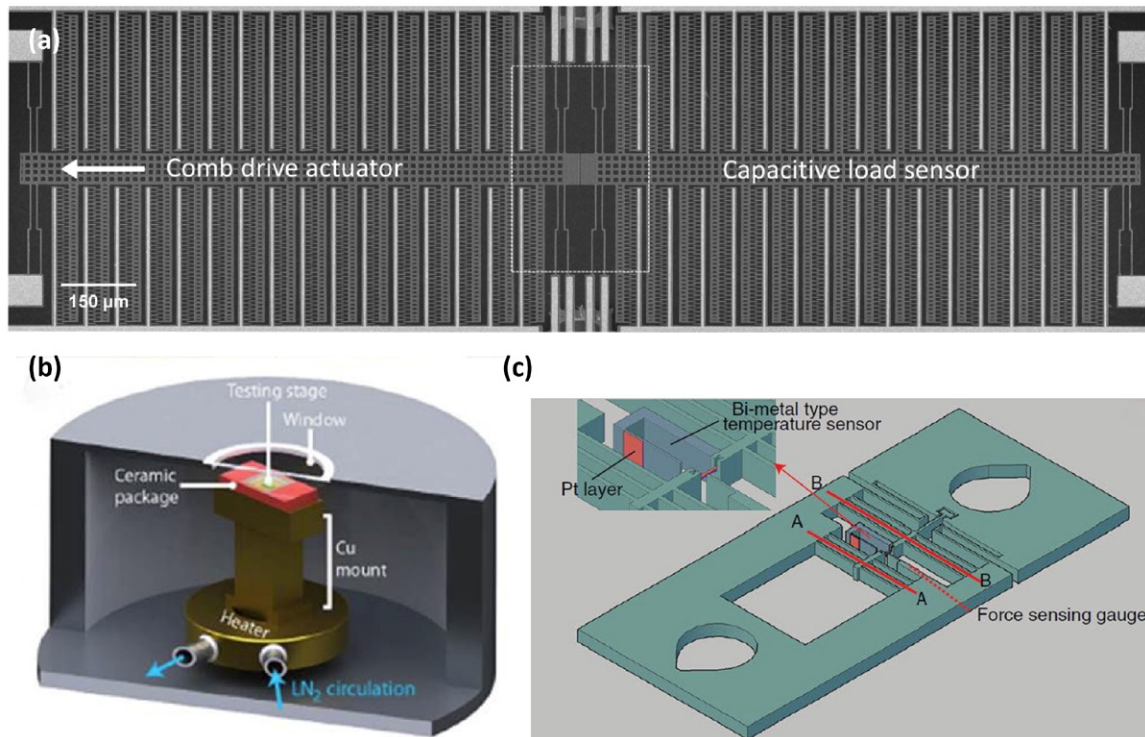


Figure 8. (a) SEM image of a MEMS thermomechanical testing platform including an on-chip heater based on Joule heating [121]. (b) Schematic of the vacuum cryostat system for temperature control. Reprinted with permission from [122]. Copyright 2014, AIP Publishing LLC. (c) Schematic of a MEMS thermomechanical platform made of SiC including a co-fabricated temperature sensor. Reprinted with permission from [123]. Copyright 2011, IOP Publishing.

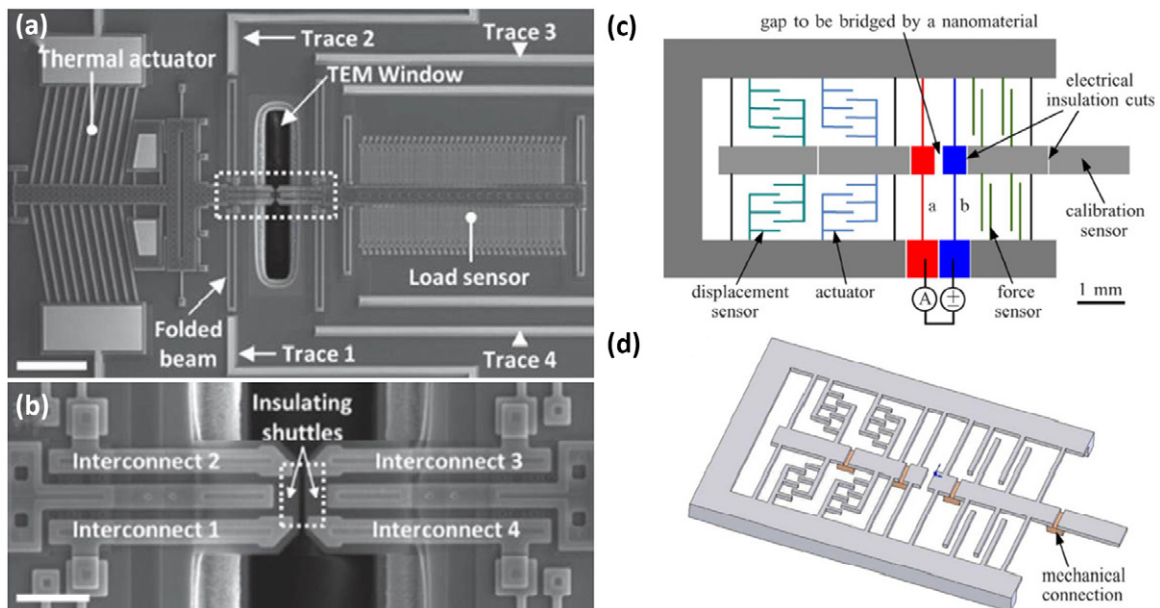


Figure 9. (a) SEM image of a MEMS platform with four-point electric measurement of a single NW. (b) Interconnects sit on the silicon nitride shuttle-provided electrical connection (magnified view of the box in panel (a)). Reprinted with permission from [125]. Copyright 2010, John Wiley and Sons. (c) Schematic of a MEMS platform with two-point electrical measurement. (d) 3D schematic of the platform showing the buried oxide layer beneath the device serving as the mechanical connection and electrical isolation. Reprinted with permission from [76]. Copyright 2011, IEEE.

in figures 9(a) and (b). Penta-twinned Ag NWs and Si NWs were tested as representatives of metallic and semiconductor NWs, respectively.

Zhang *et al* [76] fabricated an electromechanical MEMS platform based on the standard SOI process, but with a SiO₂

layer beneath the structural layer for insulation, as shown in figures 9(c) and (d). The piezoresistivity of Si NWs was reported. Kiuchi *et al* fabricated an electromechanical MEMS platform based on their previous mechanical platform [126]. An external Kelvin bridge method was used for resistance measurement.

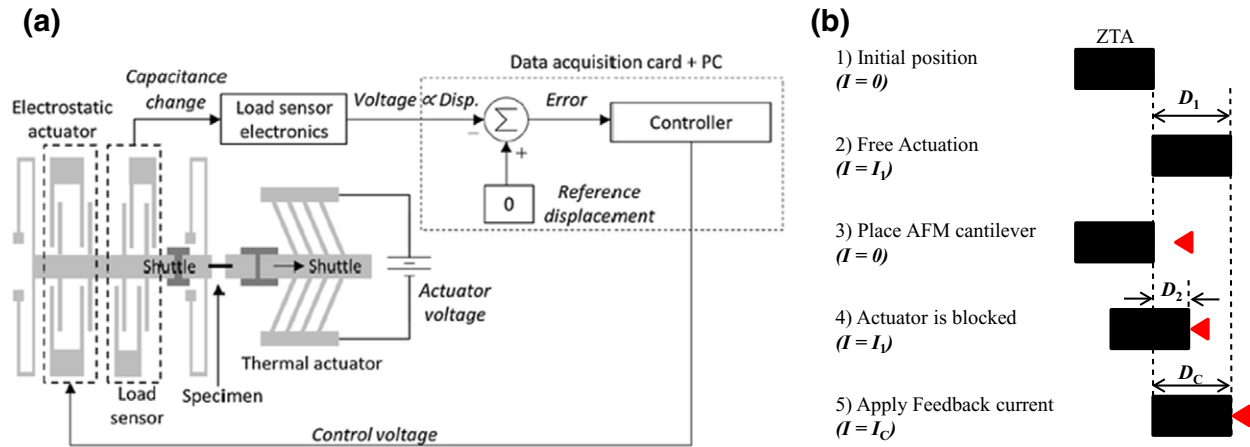


Figure 10. (a) Working principle of a MEMS platform with feedback control based on capacitive sensing. Reprinted with permission from [80]. Copyright 2014, Springer. (b) Calibration scheme for feedback control of a MEMS platform based on piezoresistive sensing [58].

Murphy *et al* have studied thermal conductivity of Si NWs as a function of tensile strain [127]. While the MEMS platform was used to apply tensile strain to the specimen, Raman spectroscopy was used to measure its thermal conductivity. Using photoluminescence and Raman spectroscopy, the optomechanical behavior of direct-bandgap NWs has been investigated [97, 128, 129]. Of note is that most MEMS-based *in situ* testing has been performed inside SEM or TEM. The integration of MEMS platforms with other types of microscopy or spectroscopy could offer exciting opportunities for multiphysical testing of nanostructures especially strain engineering.

3.5. Platforms with feedback control

One drawback of all of the MEMS platforms discussed so far is that they cannot perform true displacement-controlled loading, like the Instron or MTS machines. MEMS load sensors are made of flexible beams; no matter which sensing mechanism is used, the flexible beams deform in response to the load applied on the specimen. When a specimen undergoes strain-softening events such as phase transformation or yielding that is often accompanied with a sudden load drop, the elastic energy accumulated in the load sensor could be released, causing a drastic increment of specimen elongation even without any further loading and thus premature failure of the specimen. To prevent that from happening, the load sensor should maintain its equilibrium position during loading, which can be achieved by feedback control. In feedback control, an extra load is applied to the load sensor to keep it stationary. This extra load is recorded as the load applied to the specimen. Capacitive and piezoresistive sensors have been recently demonstrated with feedback control.

Feedback control on differential capacitive sensors has been employed in the accelerometers of analog devices (e.g. ADXL-50). However, it is not trivial to achieve that in custom-made MEMS testing platforms. Guan and Zhu [130] imposed a feedback voltage directly on the movable plate in the differential capacitive sensor to generate an electrostatic force to counterbalance the sensor displacement with the

feedback response in the order of milliseconds. Pantano *et al* introduced an additional electrostatic actuator to provide the feedback force, as shown in figure 10(a) [80], which processes a response time of 40 ms and could hold a load sensor within a range of 20 nm. The additional actuator was connected to the load sensor mechanically but isolated electrically. A feedback voltage in response to the capacitance difference (due to the applied load) was applied to the additional actuator for pulling back the load sensor to the initial position. Since the thermal actuator has a much larger stiffness than the specimen and load sensor, true displacement control was achieved. The feedback system was used for *in situ* SEM tensile testing of penta-twinned Ag NWs. A sudden drop in stress as a result of yielding was captured in the stress–strain curve, which was not observed previously [131].

Piezoresistive sensing has been explored for feedback control too. Guan and Zhu introduced a Z-shaped thermal actuator that is very compliant compared to the V-shaped one [57]. Z-shaped thermal actuators made of Si exhibited pronounced piezoresistivity [58]. The concept of feedback control of the Z-shaped thermal actuator, which is illustrated in figure 10(b), is that when the actuator is pushed back by an external force, a feedback current can be applied on the actuator to counterbalance the external force and keep it at the initial position. The feedback control was demonstrated by holding the actuator at a constant position under various external forces under quasi-static loading, with errors less than 10%. Messenger *et al* [132] reported another example of utilizing a piezoresistive sensor for feedback control in order to achieve the precision control of actuator displacement. A Wheatstone bridge was used for resistance measurement to reduce the noise level. With the feedback control, the thermal actuator was demonstrated to achieve an accuracy of 29 nm.

4. Selected results from MEMS-based nanomechanical testing

The ‘smaller is stronger’ phenomenon was first discovered for micro-whiskers in the 1950s [133] and has received extensive attention in the past decade [134–137]. In the case of metals,

as the size shrinks from the micro- to nano-scale, the dominant deformation mechanism transits from dislocation multiplication through the operation of single-arm resources to surface dislocation nucleation [1, 13, 14, 138–140]. In addition to a strong size effect on plasticity and fracture, the size effect on elasticity has been reported for some NWs [141]. MEMS-based testing platforms have been playing an instrumental role in facilitating the recent advance of nanomechanics. They have been used to test a broad range of nanostructures (e.g. carbon nanotubes, crystalline NWs, metallic glass NWs [142], and polymer nanofibers [47, 70]), under a variety of microscopes or spectroscopies (e.g. optical, SEM, TEM and Raman). Below we discuss a few representative works to highlight the diverse capabilities of MEMS platforms.

Naraghi *et al* have studied the mechanical behavior of PAN nanofibers *in situ* under an optical microscope [47]. At a nominal strain rate of $2.5 \times 10^{-3} \text{ s}^{-1}$, a Young's modulus of $7.6 \pm 1.5 \text{ GPa}$ was reported. Thinner nanofibers showed higher strengths but reduced ductility compared to thicker fibers, suggesting that thinner fibers are characterized by enhanced molecular alignment induced during electrospinning. A major benefit of this method is that strain rate experiments can be conducted and the maximum loading rate is limited by the frame rate of the camera. Naturally the authors have studied the mechanical behavior and failure of PAN nanofibers as a function of strain rate (from 2.5×10^{-4} to $2.5 \times 10^{-2} \text{ s}^{-1}$) [70]. At the fast rate, the nanofibers exhibited relatively large ductility, originated in the formation of a cascade of ripples (necks) (figure 11(a)); at the slow strain rate, the nanofibers deformed homogeneously allowing for the largest engineering strengths and extension ratios (figure 11(b)).

Time-dependent mechanical behavior is of interest not only to polymers but also to metals. Plastic deformation in metals generally consists of two components, the athermal component and the thermal component, with the latter accounting for thermally activated processes that are usually sensitive to temperature and strain rate. Recently Qin *et al* reported the time-dependent mechanical response of penta-twinned Ag NWs that include five twin boundaries running along the NW length [93]. Penta-twinned Ag NWs exhibit some interesting mechanical properties such as the size effect in yield strength and elastic modulus, strain hardening, and nucleation-controlled distributed plasticity [32, 131]. Qin *et al* discovered an unusual, fully reversible plasticity, which does not exist in single-crystalline Ag NWs. *In situ* SEM and TEM tensile testing was performed including several steps as shown in figure 11(c). A specimen was first stretched to a given strain. When the actuator was held constant, the load on the specimen decreased with time, while the specimen was elongated simultaneously. After the relaxation step, the specimen was gradually unloaded until the actuator was turned off (the specimen was still elongated but under compressive stress). At the recovery step, complete strain recovery was observed. Molecular dynamics simulations revealed that the observed behavior originates from the surface nucleation, propagation and retraction of partial dislocations. More specifically, vacancies reduce the dislocation nucleation barrier, facilitating stress relaxation, while the twin boundaries and their intrinsic

stress field promote retraction of partial dislocations, resulting in full strain recovery. *In situ* TEM directly observed the interaction between dislocations and existing twin boundaries during the relaxation step and the dislocation annihilation during the recovery step, as shown in figure 11(d). Since the relaxation strain is rather small, a highly stable testing system (e.g. the MEMS platform used) is the key to observing such a fine behavior. Other testing systems such as those involving a nanomanipulator might not work due to the inevitable drift of the nanomanipulator. Similar recoverable plasticity on penta-twinned Ag NWs has been reported in terms of athermal manifestation [143].

Fatigue is another important cycle-dependent (potentially time-dependent) mechanical behavior but so far has only received limited attention, mainly due to instrumentation difficulties. Using the 'two-sensor' platform, Hosseini and Pierron have investigated the fatigue of Au nanobeams [95]. The specimens were $1.5 \mu\text{m}$ in width, $20 \mu\text{m}$ in length and 100 nm in thickness, and the grain size ranged from 10 to 400 nm . Fatigue tests were carried out both *ex situ* and *in situ* TEM. For the *ex situ* test at ambient environment, the thermal actuator was cycled between 0.4 and 1.8 V in steps of 0.1 V at a frequency of 0.07 Hz . The specimen failed after $11\,125$ cycles and a ratcheting behavior was observed, as shown in figure 11(e). The maximum strain increased from 1.0% to 1.4% with loading times, and the maximum stress decreased from 0.62 to 0.54 GPa . No obvious change in the microstructure was observed from post-mortem TEM images. Next *in situ* TEM fatigue testing was performed to observe the microstructure evolution. The actuation voltage was cycled between 0 and 4 V in steps of 0.4 V at a frequency of 0.25 Hz . The specimen failed at 6995 cycles and the same ratcheting behavior was observed again. Figure 11(f) shows a TEM image of specimen after fracture, where large numbers of dislocations can be seen near the fracture plane as indicated by the green rectangle. In addition, the blue rectangle shows the initiation of surface cracks adjacent to the fatigue crack. During the *in situ* TEM test, a large number of dislocations were found to nucleate after 400 cycles, accompanied with twins and stacking faults. This work demonstrated that a MEMS platform with two electronic sensors can be a promising tool to investigate fatigue at the nanoscale.

There has been increasing evidence suggesting the size dependence of the brittle to ductile transition (BDT) of Si. The transition temperature has been reported to decrease from $\sim 940^\circ\text{C}$ at bulk [144] to 400°C at microscale [145, 146], and even lower to $\sim 300^\circ\text{C}$ at sub-microscale [45]. The systematic investigation of the BDT of Si as a function of size, however, is still lacking especially at the nanoscale. Kang and Saif reported temperature-dependent Young's modulus in Si beams with a cross-sectional area of $20.68 \mu\text{m}^2$ under uniaxial tensile loading from room temperature to 403°C [123]. Later, using a similar device, they observed the transition temperatures of Si beams under bending that reduced from 375°C to 293°C while beam width decreased from $8.7 \mu\text{m}$ to 720 nm [45], as shown by the force-displacement behavior in figure 12(a). Figure 12(b) shows a SEM image of a fractured Si beam with obvious plastic deformation. Chang and

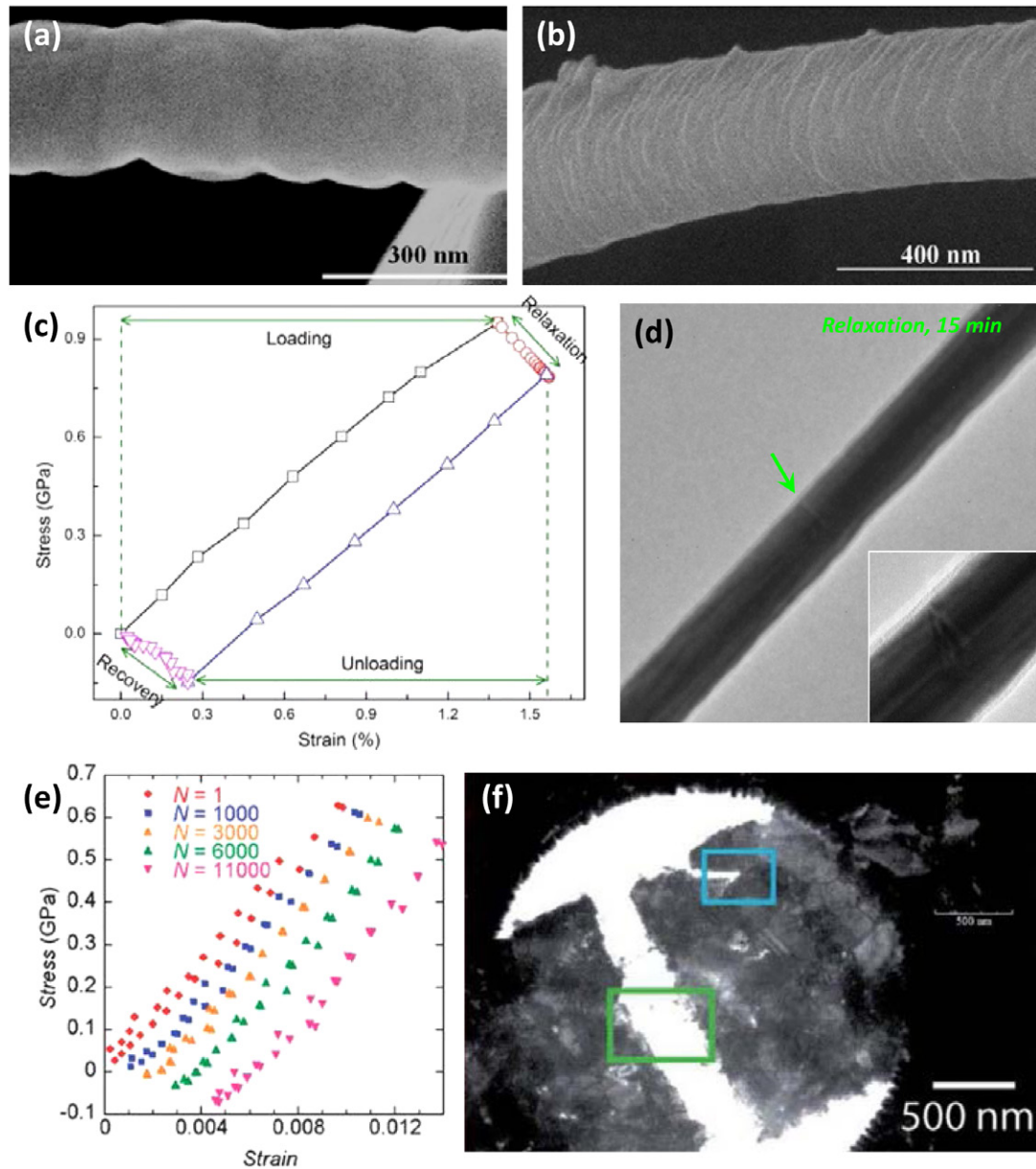


Figure 11. (a) SEM images of deformed PAN nanofibers at strain rates of $2.5 \times 10^{-2} \text{ s}^{-1}$ (a) and $2.5 \times 10^{-4} \text{ s}^{-1}$ (b). (a) and (b) reprinted with permission from [70]. Copyright 2007, AIP Publishing LLC. (c) Stress–strain curve of a penta-twinned Ag NW during loading, relaxation, unloading and recovery [93]. (d) TEM image revealing dislocation nucleation and interaction with the twin boundaries during the relaxation of the penta-twinned Ag NW [93]. (e) Stress–strain behavior of Au nanobeam under cyclic loading. (f) TEM image of the fracture surface of the Au nanobeam after fatigue failure. Reprinted with permission from [95]. Copyright 2013, Royal Society of Chemistry.

Zhu reported the first evidence of BDT of Si NWs under tension [121]. A single-crystalline Si NW of 60 nm in diameter was tested initially at room temperature and then at gradually increasing temperatures. At room temperature and 362 K, a linear elastic stress–strain behavior was measured. But at 399 K, 0.5% plastic strain was measured when the NW was totally unloaded, which indicates that the BDT temperature of this NW was between 362 and 399 K, much lower than that of single-crystalline Si at bulk and microscale, see figure 12(d). The NW was broken at 599 K with a failure strain of 4.9%, substantially higher than that at room temperature. The fracture surfaces, as shown in figure 12(c), indicates a shear

fracture plane, which agrees well with the molecular dynamics prediction for $\langle 110 \rangle$ -oriented Si NWs [147].

Zhang *et al* utilized a MEMS platform to measure the piezoresistivity of Si NWs using two-point electric measurement [76]. Strain dependent resistance was found in a Si NW under 100 nm, which reduced from $5.9 \times 10^{11} \Omega$ at strain free to $2.2 \times 10^{10} \Omega$ at 3.0% strain, as shown in the I – V curve in figure 13(a). To eliminate the influence of contact resistance in the two-point electric measurement [76, 96], Bernal *et al* recently measured the resistances of Si and Ag NWs under mechanical strain using a MEMS platform with four-point electric measurement. For Ag NWs, the resistance exhibited

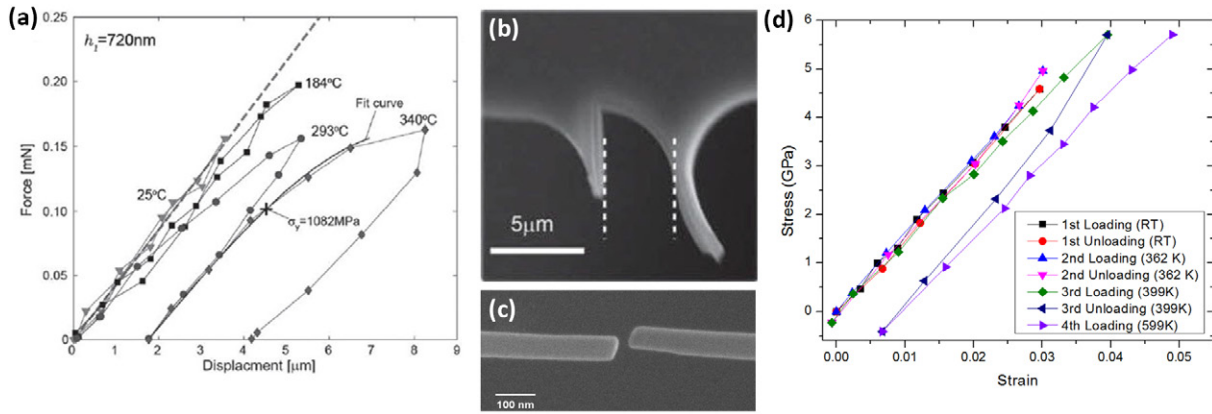


Figure 12. (a) Bending behavior of a 720 nm thickness silicon beam at different temperatures. (b) SEM image of the fractured Si beams showing plastic deformation under bending at elevated temperature. Reprinted with permission from [45]. Copyright 2013, John Wiley and Sons. (c) Tensile behavior of a Si NW at different temperatures [121]. (d) SEM image of the Si NW fractured at 600 K showing shear failure [121].

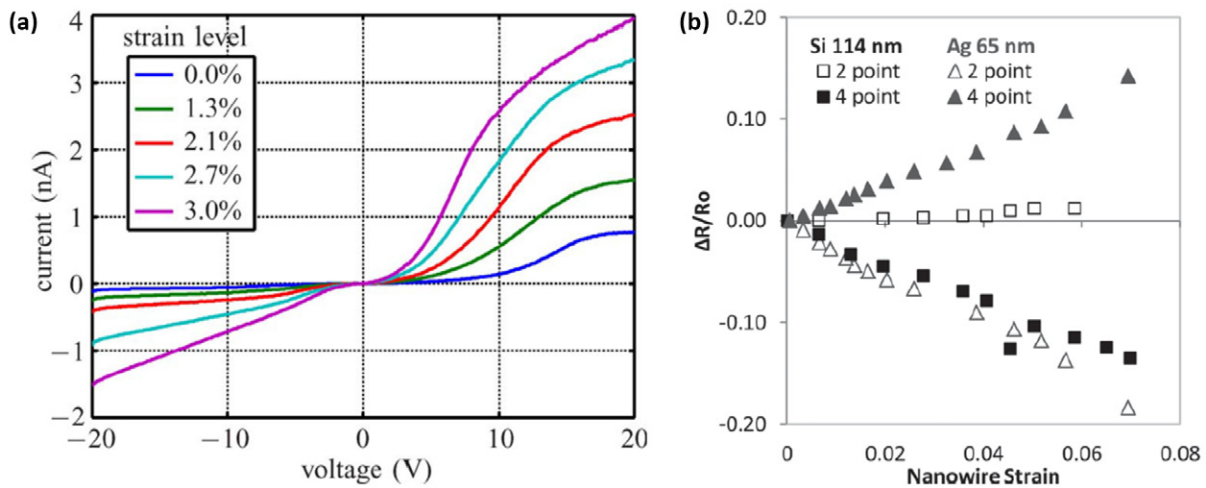


Figure 13. (a) I - V curve of Si NW at different strain levels using two-point electrical measurement. Reprinted with permission from [76]. Copyright 2011, IEEE. (b) Strain-dependent electromechanical response of Ag and Si NWs. Reprinted with permission from [125]. Copyright 2013, John Wiley and Sons.

size dependence, increasing with decreasing diameter, due to the enhancement of surface scattering. Changes in resistance with applied strain were found to be due to dimensional changes. For Si NWs, a reduction of resistance due to applied strain was observed, as shown in figure 13(b), which is consistent with the piezoresistance behavior of bulk silicon [148]. The first order piezoresistive coefficients were found to be of similar magnitude as the bulk value. This result is in contrast to the giant piezoresistivity reported for Si NWs [96]. Indeed the giant piezoresistivity of Si NWs remains a matter of debate. The literature indicates that reproducible evidence for giant piezoresistance in ungated nanowires is limited; but in gated nanowires, giant piezoresistance has been reproduced [149].

MEMS offer promising potential for multiphysical testing of nanostructures especially strain engineering. For instance, Murphy *et al* have combined a MEMS tensile device with Raman spectroscopy to study the stress-dependent thermal conductivity of Si NWs [127]. Thermal conductivity was measured by varying the laser power and the distance from the laser spot to the clamps with the assistance of a heat transfer

model. It was found that tensile stress of 1.7 GPa only caused a small change in thermal conductivity. However, when a large density of defects was introduced in NWs by ion irradiation of Ga^+ , a drastic decrease in thermal conductivity ($>90\%$) was found, which was attributed to enhanced phonon scattering.

Another example of strain engineering is optomechanical behavior. Greil *et al* applied uniaxial tensile strain on Ge NWs while recording the photocurrent using Raman spectroscopy simultaneously [97]. The photocurrent spectra of Ge NWs was found to shift toward higher wavelengths with increasing tensile stress showing a linear dependence. The results indicated the lowering of the direct bandgap energy due to tensile stress. Signorello *et al* also discovered a large bandgap shift in wurtzite GaAs NWs under both tensile and compressive strains [128]. Tensile and compressive stresses decrease and increase the phonon energy, respectively, and thus photoluminescence and Raman spectra shift accordingly. While in both cases above no true MEMS devices were used, MEMS devices are expected to play an important role in strain engineering.

5. Summary and outlook

We have reviewed the exciting advances in the field of mechanical characterization of 1D nanostructures using MEMS platforms in the past decade. Many different types of MEMS platforms have been designed, fabricated and employed for nanomechanical characterizations ranging from basic tensile testing to fatigue to thermomechanical testing and multiphysical testing. A large number of nanostructures have been characterized including carbon nanotubes, crystalline NWs, metallic glass NWs, and polymer nanofibers. MEMS platforms and related nanomechanics studies have contributed tremendously to our understanding of the nanoscale mechanical behaviors.

It remains a great challenge to manipulate and position individual nanostructures onto the MEMS platforms with high yield and high throughput. Novel nanorobotic manipulation or synthesis methods for preparing nanostructure specimens should be sought to overcome this bottleneck. Feedback control has been successfully demonstrated to capture strain-softening behavior. But higher spatial resolution and faster response are still needed. MEMS-based platforms and related testing methods have seen rapid progress in the past decade. For the further growth of the field, it is an important step to develop standards commensurate with those at larger scales.

Since MEMS-based nanomechanical testing is typically performed *in situ* in SEM and TEM, possible irradiation damage due to the electron beam should be considered. Irradiation damage could include heating, electrostatic charging, ionization damage (radiolysis), displacement damage, sputtering and hydrocarbon contamination [150], depending on the acceleration voltage, beam density, exposure time and observed material. For instance, electron-beam-assisted super-plastic shaping of nanoscale amorphous silica under 200 keV in TEM has been reported [151].

In the past decade, surface effects on NW mechanical behaviors have attracted tremendous interests. It will be useful to understand the role of internal microstructures/boundaries for the mechanical properties of NWs, e.g. is there coupling between free surfaces and internal defects/boundaries? Nanostructures synthesized by various ‘bottom-up’ methods often possess internal defects and/or boundaries. For instance, solution synthesized Ag NWs possess interesting pentatwinned structures, with five twin boundaries along the NW length [93]. Vapor–liquid–solid synthesized SiC NWs possess rather complicated microstructures, e.g. 3C structure with an inclined stacking fault and highly defective structure [79]. In vapor–liquid–solid synthesis, doping typically occurs either intentionally or unintentionally [152]. Internal defect structures must be carefully characterized before the testing results can be interpreted accurately.

With the advance of nanodevices, 1D nanostructures including NWs as building blocks will undergo more and more realistic mechanical loadings. Therefore, it is of critical relevance to study other effects (e.g. time, temperature and environment) on their mechanical behaviors. For example, creep, stress relaxation and fatigue properties will be important

for long-time operation and reliability of the nanodevices. Strain rate, temperature and relaxation transient tests can be used to probe thermally activated mechanisms. MEMS will undoubtedly play an important role in such studies.

Due to its tiny size, a MEMS platform fits easily for *in situ* SEM/TEM testing. With the recent advance in time-resolved electron microscopy [153] (e.g. dynamic transmission electron microscopy, DTEM [154]), it might become possible to capture the dynamic response of nanostructures with atomic resolution. Combination of MEMS platforms and DTEM, together with the limited volume of 1D nanostructures, could offer exciting opportunities for probing the nanoscale mechanical and structural behaviors. Beyond microscopy (e.g. SEM/TEM/AFM/optical), it is promising to combine MEMS platforms with spectroscopy for multiphysical testing. For instance, Raman spectroscopy is commonly used to observe vibrational modes in molecules. Micro-Raman has been used to measure temperature, stress, phase transformation, etc. with spatial resolution of around 1 μm [155]. Photoluminescence spectroscopy can be used to measure the bandgap of semiconductors.

Acknowledgments

Financial support by the National Science Foundation (NSF) through award No. CMMI-1301193 and DMR-1410475 is gratefully acknowledged.

References

- [1] Zhu T and Li J 2010 Ultra-strength materials *Prog. Mater. Sci.* **55** 710–57
- [2] Wang Z L and Song J 2006 Piezoelectric nanogenerators based on zinc oxide nanowire arrays *Science* **312** 242–6
- [3] Chan C K, Peng H, Liu G, McIlwrath K, Zhang X F, Huggins R A and Cui Y 2008 High-performance lithium battery anodes using silicon nanowires *Nat. Nano* **3** 31–5
- [4] Liu X H *et al* 2012 *In situ* atomic-scale imaging of electrochemical lithiation in silicon *Nat. Nanotechnol.* **7** 749–56
- [5] Feng X, He R, Yang P and Roukes M 2007 Very high frequency silicon nanowire electromechanical resonators *Nano Lett.* **7** 1953–9
- [6] Loh O Y and Espinosa H D 2012 Nanoelectromechanical contact switches *Nat. Nanotechnol.* **7** 283–95
- [7] McAlpine M C, Friedman R S, Jin S, Lin K, Wang W U and Lieber C M 2003 High-performance nanowire electronics and photonics on glass and PLASTIC substrates *Nano Lett.* **3** 1531–5
- [8] Fan Z, Ho J C, Takahashi T, Yerushalmi R, Takei K, Ford A C, Chueh Y-L and Javey A 2009 Toward the development of printable nanowire electronics and sensors *Adv. Mater.* **21** 3730–43
- [9] Ryu S Y, Xiao J, Park W Il, Son K S, Huang Y Y, Paik U and Rogers J A 2009 Lateral buckling mechanics in silicon nanowires on elastomeric substrates *Nano Lett.* **9** 3214–9
- [10] Xu F, Lu W and Zhu Y 2011 Controlled 3D buckling of silicon nanowires for stretchable electronics *ACS Nano* **5** 672–8
- [11] Yao S and Zhu Y 2015 Nanomaterial-enabled stretchable conductors: strategies, materials and devices *Adv. Mater.* **27** 1480–511

- [12] Zhu Y, Xu F, Qin Q, Fung W Y and Lu W 2009 Mechanical properties of vapor–liquid–solid synthesized silicon nanowires *Nano Lett.* **9** 3934–9
- [13] Greer J R and De Hosson J T M 2011 Plasticity in small-sized metallic systems: intrinsic versus extrinsic size effect *Prog. Mater. Sci.* **56** 654–724
- [14] Weinberger C R and Cai W 2012 Plasticity of metal nanowires *J. Mater. Chem.* **22** 3277
- [15] Zhu Y, Ke C and Espinosa H D 2007 Experimental techniques for the mechanical characterization of 1D nanostructures *Exp. Mech.* **47** 7–24
- [16] Gianola D S and Eberl C 2009 Micro-and nanoscale tensile testing of materials *JOM* **61** 24
- [17] Robertson I M *et al* 2011 Towards an integrated materials characterization toolbox *J. Mater. Res.* **26** 1341–83
- [18] Robertson I M, Ferreira P J, Dehm G, Hull R and Stach E A 2008 Visualizing the behavior of dislocations—seeing is believing *MRS Bull.* **33** 122–31
- [19] Poncharal P, Wang Z L, Ugarte D and Heer W De 1999 Electrostatic deflections and electromechanical resonances of carbon nanotubes *Science* **283** 1513–6
- [20] Treacy M M J, Ebbesen T W and Gibson J M 1996 Exceptionally high Young's modulus observed for individual carbon nanotubes *Nature* **381** 678–80
- [21] Qin Q, Xu F, Cao Y, Ro P I and Zhu Y 2012 Measuring true Young's modulus of a cantilevered nanowire: effect of clamping on resonance frequency *Small* **8** 2571–6
- [22] Chen C, Shi Y, Zhang Y, Zhu J and Yan Y 2006 Size dependence of Young's modulus in ZnO nanowires *Phys. Rev. Lett.* **96** 075505
- [23] Bai X D, Gao P X, Wang Z L and Wang E G 2003 Dual-mode mechanical resonance of individual ZnO nanobelts *Appl. Phys. Lett.* **82** 4806
- [24] Wong E, Sheehan P and Lieber C M 1997 Nanobeam mechanics: elasticity, strength, and toughness of nanorods and nanotubes *Science* **277** 1971–5
- [25] Wu B, Heidelberg A and Boland J J 2005 Mechanical properties of ultrahigh-strength gold nanowires *Nat. Mater.* **4** 525–9
- [26] Salvétat J-P, Briggs G, Bonard J-M, Bacsá R, Kulik A, Stöckli T, Burnham N and Forró L 1999 Elastic and shear moduli of single-walled carbon nanotube ropes *Phys. Rev. Lett.* **82** 944–7
- [27] Zheng Y, Geer R E, Dovidenko K, Kopycinska-Müller M and Hurley D C 2006 Quantitative nanoscale modulus measurements and elastic imaging of SnO₂ nanobelts *J. Appl. Phys.* **100** 124308
- [28] Stan G, Ciobanu C V, Parthangal P M and Cook R F 2007 Diameter-dependent radial and tangential elastic moduli of ZnO nanowires *Nano Lett.* **7** 3691–7
- [29] Zheng M, Ke C, Bae I-T, Park C, Smith M W and Jordan K 2012 Radial elasticity of multi-walled boron nitride nanotubes *Nanotechnology* **23** 95703
- [30] Yu M-F, Lourie O, Dyer M J, Moloni K, Kelly T F and Ruoff R S 2000 Strength and breaking mechanism of multiwalled carbon nanotubes under tensile load *Science* **287** 637–40
- [31] Xu F, Qin Q, Mishra A, Gu Y and Zhu Y 2010 Mechanical properties of ZnO nanowires under different loading modes *Nano Res.* **3** 271–80
- [32] Zhu Y, Qin Q, Xu F, Fan F, Ding Y, Zhang T, Wiley B J and Wang Z L 2012 Size effects on elasticity, yielding, and fracture of silver nanowires: *in situ* experiments *Phys. Rev. B* **85** 045443
- [33] He M-R, Shi Y, Zhou W, Chen J W, Yan Y J and Zhu J 2009 Diameter dependence of modulus in zinc oxide nanowires and the effect of loading mode: *in situ* experiments and universal core-shell approach *Appl. Phys. Lett.* **95** 091912
- [34] Lin C-H, Ni H, Wang X, Chang M, Chao Y J, Deka J R and Li X 2010 *In situ* Nanomechanical characterization of single-crystalline boron nanowires by buckling *Small* **6** 927–31
- [35] Richter G, Hillerich K, Gianola D S, Mönig R, Kraft O and Volkert C A 2009 Ultrahigh strength single crystalline nanowhiskers grown by physical vapor deposition *Nano Lett.* **9** 3048–52
- [36] Li X, Gao H, Murphy C J and Caswell K K 2003 Nanoindentation of silver nanowires *Nano Lett.* **3** 1495–8
- [37] Feng G, Nix W D, Yoon Y and Lee C J 2006 A study of the mechanical properties of nanowires using nanoindentation *J. Appl. Phys.* **99** 074304
- [38] Haque M A, Espinosa H D and Lee H 2010 MEMS for *in situ* testing—handling, actuation, loading, and displacement measurements *MRS Bull.* **35** 375–81
- [39] Dong J, Mukhopadhyay D and Ferreira P M 2007 Design, fabrication and testing of a silicon-on-insulator (SOI) MEMS parallel kinematics XY stage *J. Micromech. Microeng.* **17** 1154–61
- [40] Beyeler F, Neild A, Oberti S, Bell D J, Sun Y, Dual J and Nelson B J 2007 Monolithically fabricated microgripper with integrated force sensor for manipulating microobjects and biological cells aligned in an ultrasonic field *J. Microelectromech. Syst.* **16** 7–15
- [41] Zhu Y, Corigliano A and Espinosa H D 2006 A thermal actuator for nanoscale *in situ* microscopy testing: design and characterization *J. Micromech. Microeng.* **16** 242–53
- [42] Zhu Y and Espinosa H D 2005 An electromechanical material testing system for *in situ* electron microscopy and applications *Proc. Natl Acad. Sci. USA* **102** 14503–8
- [43] Zhu Y, Moldovan N and Espinosa H D 2005 A microelectromechanical load sensor for *in situ* electron and x-ray microscopy tensile testing of nanostructures *Appl. Phys. Lett.* **86** 013506
- [44] Espinosa H D, Zhu Y and Moldovan N 2007 Design and operation of a MEMS-based material testing system for nanomechanical characterization *J. Microelectromech. Syst.* **16** 1219–31
- [45] Kang W and Saif M T A 2013 *In situ* study of size and temperature dependent brittle-to-ductile transition in single crystal silicon *Adv. Funct. Mater.* **23** 713–9
- [46] Samuel B A, Haque M A, Yi B, Rajagopalan R and Foley H C 2007 Mechanical testing of pyrolysed poly-furfuryl alcohol nanofibres *Nanotechnology* **18** 115704
- [47] Naraghi M, Chasiotis I, Kahn H, Wen Y and Dzenis Y 2007 Novel method for mechanical characterization of polymeric nanofibers *Rev. Sci. Instrum.* **78** 085108
- [48] Williams P A, Papadakis S J, Falvo M R, Patel A M, Sinclair M, Seeger A, Helser A, Taylor R M, Washburn S and Superfine R 2002 Controlled placement of an individual carbon nanotube onto a microelectromechanical structure *Appl. Phys. Lett.* **80** 2574
- [49] Haque M A and Saif M T A 2002 *In situ* tensile testing of nano-scale specimens in SEM and TEM *Exp. Mech.* **42** 123–8
- [50] Kang W and Saif M T A 2010 A novel method for *in situ* uniaxial tests at the micro/nano scale—part I: theory *J. Microelectromech. Syst.* **19** 1309–21
- [51] Kovacs G T A 1998 *Micromachined Transducers Sourcebook* (Boston: McGraw-Hill)
- [52] Liu C 2011 *Foundation of MEMS* (Englewood Cliffs, NJ: Prentice Hall)
- [53] Tang W C, Nguyen T C H and Howe R T 1989 Laterally driven polysilicon resonant microstructures *Sensors Actuators* **20** 25–32
- [54] Kahn H, Ballarini R, Mullen R L and Heuer A H 1999 Electrostatically actuated failure of microfabricated

- polysilicon fracture mechanics specimens *Proc. R. Soc. A: Math. Phys. Eng. Sci.* **455** 3807–23
- [55] Huang Q-A and Lee N K S 1999 Analysis and design of polysilicon thermal flexure actuator *J. Micromech. Microeng.* **9** 64–70
- [56] Que L, Park J-S and Gianchandani Y B 2001 Bent-beam electrothermal actuators-part I: single beam and cascaded devices *J. Microelectromech. Syst.* **10** 247–54
- [57] Guan C and Zhu Y 2010 An electrothermal microactuator with Z-shaped beams *J. Micromech. Microeng.* **20** 085014
- [58] Ouyang J and Zhu Y 2012 Z-shaped MEMS thermal actuators: piezoresistive self-sensing and preliminary results for feedback control *J. Microelectromech. Syst.* **21** 596–604
- [59] Qin Q and Zhu Y 2013 Temperature control in thermal microactuators with applications to *in situ* nanomechanical testing *Appl. Phys. Lett.* **102** 013101
- [60] Pant B, Choi S, Baumert E K, Allen B L, Graham S, Gall K and Pierron O N 2012 MEMS-based nanomechanics: influence of MEMS design on test temperature *Exp. Mech.* **52** 607–17
- [61] Abbas K, Alaie S and Leseman Z C 2012 Design and characterization of a low temperature gradient and large displacement thermal actuators for *in situ* mechanical testing of nanoscale materials *J. Micromech. Microeng.* **22** 125027
- [62] Boser B E and Howe R T 1996 Surface micromachined accelerometers *IEEE J. Solid-State Circuits* **31** 366–75
- [63] Pant B, Allen B L, Zhu T, Gall K and Pierron O N 2011 A versatile microelectromechanical system for nanomechanical testing *Appl. Phys. Lett.* **98** 053506
- [64] Zhang D, Drissen W, Breguet J-M, Clavel R and Michler J 2009 A high-sensitivity and quasi-linear capacitive sensor for nanomechanical testing applications *J. Micromech. Microeng.* **19** 075003
- [65] Barlian A A, Park W-T, Mallon J R, Rastegar A J and Pruitt B L 2009 Review: semiconductor piezoresistance for microsystems *Proc. IEEE. Inst. Electr. Electron. Eng.* **97** 513–52
- [66] Saif M T A and MacDonald N C 1996 A millinewton microloading device *Sensors Actuators* **52** 65–75
- [67] Corigliano A, de Masi B, Frangi A, Comi C, Villa A and Marchi M 2004 Mechanical characterization of polysilicon through on-chip tensile tests *J. Microelectromech. Syst.* **13** 200–19
- [68] Corigliano A, Domenella L and Langfelder G 2010 On-chip mechanical characterization using an electro-thermo-mechanical actuator *Exp. Mech.* **50** 695–707
- [69] Lu S, Dikin D A, Zhang S, Fisher F T, Lee J and Ruoff R S 2004 Realization of nanoscale resolution with a micromachined thermally actuated testing stage *Rev. Sci. Instrum.* **75** 2154
- [70] Naraghi M, Chasiotis I, Kahn H, Wen Y and Dzenis Y 2007 Mechanical deformation and failure of electrospun polyacrylonitrile nanofibers as a function of strain rate *Appl. Phys. Lett.* **91** 151901
- [71] Kiuchi M, Matsui S and Isono Y 2007 Mechanical characteristics of FIB deposited carbon nanowires using an electrostatic actuated nano tensile testing device *J. Microelectromech. Syst.* **16** 191–201
- [72] Ganesan Y, Lu Y, Peng C, Hao L, Ballarini R and Lou J 2010 Development and application of a novel microfabricated device for the *in situ* tensile testing of 1D nanomaterials *J. Microelectromech. Syst.* **19** 675–82
- [73] Samuel B A, Desai A V and Haque M A 2006 Design and modeling of a MEMS pico-Newton loading/sensing device *Sensors Actuators* **127** 155–62
- [74] Tsuchiya T, Ura Y, Sugano K and Tabata O 2012 Electrostatic tensile testing device with nanonewton and nanometer resolution and its application to nanowire testing *J. Microelectromech. Syst.* **21** 523–9
- [75] Yilmaz M and Kysar J W 2013 Monolithic integration of nanoscale tensile specimens and MEMS structures *Nanotechnology* **24** 165502
- [76] Zhang Y, Liu X, Ru C, Zhang Y L, Dong L and Sun Y 2011 Piezoresistivity characterization of synthetic silicon nanowires using a MEMS device *J. Microelectromech. Syst.* **20** 959–67
- [77] Brown J J, Suk J W, Singh G, Baca A I, Dikin D A, Ruoff R S and Bright V M 2009 Microsystem for nanofiber electromechanical measurements *Sensors Actuators* **155** 1–7
- [78] Steighner M S, Snedeker L P, Boyce B L, Gall K, Miller D C and Muhlstein C L 2011 Dependence on diameter and growth direction of apparent strain to failure of Si nanowires *J. Appl. Phys.* **109** 033503
- [79] Cheng G, Chang T-H, Qin Q, Huang H and Zhu Y 2014 Mechanical properties of silicon carbide nanowires: effect of size-dependent defect density *Nano Lett.* **14** 754–8
- [80] Pantano M F, Bernal R A, Pagnotta L and Espinosa H D 2015 Multiphysics design and implementation of a microsystem for displacement-controlled tensile testing of nanomaterials *Meccanica* **50** 549–60
- [81] Hazra S S, Baker M S, Beuth J L and de Boer M P 2011 Compact on-chip microtensile tester with prehensile grip mechanism *J. Microelectromech. Syst.* **20** 1043–53
- [82] Hazra S S, Baker M S, Beuth J L and de Boer M P 2009 Demonstration of an *in situ* on-chip tensile tester *J. Micromech. Microeng.* **19** 82001
- [83] De Boer M P, Corwin A D, Kotula P G, Baker M S, Michael J R, Subhash G and Shaw M J 2008 On-chip laboratory suite for testing of free-standing metal film mechanical properties, part II—experiments *Acta Mater.* **56** 3313–26
- [84] Lu S, Chung J and Ruoff R S 2005 Controlled deposition of nanotubes on opposing electrodes *Nanotechnology* **16** 1765
- [85] Brown J J, Baca A I, Bertness K A, Dikin D A, Ruoff R S and Bright V M 2011 Tensile measurement of single crystal gallium nitride nanowires on MEMS test stages *Sensors Actuators* **166** 177–86
- [86] Espinosa H D, Bernal R A and Filleter T 2012 *In situ* TEM electromechanical testing of nanowires and nanotubes *Small* **8** 3233–52
- [87] Peng B, Locascio M, Zapol P, Li S, Mielke S L, Schatz G C and Espinosa H D 2008 Measurements of near-ultimate strength for multiwalled carbon nanotubes and irradiation-induced crosslinking improvements *Nat. Nanotechnol.* **3** 626–31
- [88] Agrawal R, Peng B and Espinosa H D 2009 Experimental-computational investigation of ZnO nanowires strength and fracture *Nano Lett.* **9** 4177–83
- [89] Chen L Y, Richter G, Sullivan J P and Gianola D S 2012 Lattice anharmonicity in defect-free Pd nanowhiskers *Phys. Rev. Lett.* **109** 125503
- [90] Zhang D, Breguet J-M, Clavel R, Phillippe L, Utke I and Michler J 2009 *In situ* tensile testing of individual Co nanowires inside a scanning electron microscope *Nanotechnology* **20** 365706
- [91] Guo H, Chen K, Oh Y, Wang K, Dejoie C, Syed Asif S A, Warren O L, Shan Z W, Wu J and Minor A M 2011 Mechanics and dynamics of the strain-induced M1–M2 structural phase transition in individual VO₂ nanowires *Nano Lett.* **11** 3207–13
- [92] Murphy K F, Chen L Y and Gianola D S 2013 Effect of organometallic clamp properties on the apparent diversity of tensile response of nanowires *Nanotechnology* **24** 235704

- [93] Qin Q, Sheng Y, Cheng G, Li X, Chang T-H, Richter G, Zhu Y and Gao H 2015 Recoverable plasticity in penta-twinned metallic nanowires governed by dislocation nucleation and retraction *Nat. Commun.* **6** 5983
- [94] Ganesan Y, Peng C, Lu Y, Ci L, Srivastava A, Ajayan P M and Lou J 2010 Effect of nitrogen doping on the mechanical properties of carbon nanotubes *ACS Nano* **4** 7637–43
- [95] Hosseinian E and Pierron O N 2013 Quantitative *in situ* TEM tensile fatigue testing on nanocrystalline metallic ultrathin films *Nanoscale* **5** 12532–41
- [96] He R and Yang P 2006 Giant piezoresistance effect in silicon nanowires *Nat. Nanotechnol.* **1** 42–6
- [97] Greil J, Lugstein A, Zeiner C, Strasser G and Bertagnolli E 2012 Tuning the electro-optical properties of germanium nanowires by tensile strain *Nano Lett.* **12** 6230–4
- [98] Chu T, Ranson W and Sutton M A 1985 Applications of digital-image-correlation techniques to experimental mechanics *Exp. Mech.* **25** 232–44
- [99] Bruck H, McNeill S R, Sutton M A and Iii W P 1989 Digital image correlation using Newton–Raphson method of partial differential correction *Exp. Mech.* **29** 261–7
- [100] Sutton M A, McNeill S R, Helm J D and Chao Y J 2000 Advances in 2D and 3D computer vision *Photomechanics Topics in Applied Physics* vol 77, ed P Rastogi (Berlin: Springer) pp 323–72
- [101] Sharpe W N, Pulskamp J, Gianola D S, Eberl C, Polcawich R G and Thompson R J 2007 Strain measurements of silicon dioxide microspecimens by digital Imaging processing *Exp. Mech.* **47** 649–58
- [102] Sutton M A, Li N, Joy D C, Reynolds A. P and Li X 2007 Scanning electron microscopy for quantitative small and large deformation measurements part I: SEM imaging at magnifications from 200 to 10000 *Exp. Mech.* **47** 775–87
- [103] Sutton M A, Orteu J and Schreier H W 2009 *Image Correlation for Shape, Motion and Deformation Measurements* (New York: Springer)
- [104] Kammers A D and Daly S 2013 Digital image correlation under scanning electron Microscopy: methodology and validation *Exp. Mech.* **53** 1743–61
- [105] Naraghi M, Ozkan T, Chasiotis I, Hazra S S and de Boer M P 2010 MEMS platform for on-chip nanomechanical experiments with strong and highly ductile nanofibers *J. Micromech. Microeng.* **20** 125022
- [106] Gianola D S, Sedlmayr A, Mönig R, Volkert C A, Major R C, Cyrankowski E, Asif S A S, Warren O L and Kraft O 2011 *In situ* nanomechanical testing in focused ion beam and scanning electron microscopes *Rev. Sci. Instrum.* **82** 063901
- [107] Kang W, Han J H and Saif M T A 2010 A novel method for *in situ* uniaxial tests at the micro/nano scale—part II: experiment *Microelectromech. Syst. J.* **19** 1322–30
- [108] Hemker K J and Sharpe W N 2007 Microscale characterization of mechanical properties *Annu. Rev. Mater. Res.* **37** 93–126
- [109] Lu S, Guo Z, Ding W, Dikin D A, Lee J and Ruoff R S 2006 *In situ* mechanical testing of templated carbon nanotubes *Rev. Sci. Instrum.* **77** 125101
- [110] Oh Y, Cyrankowski E, Shan Z W and Asif S A S 2010 Micro/nano-mechanical test system employing tensile test holder with push-to-pull transformer US Patent: US20100095780 A1
- [111] Guo H, Wang K, Deng Y, Oh Y, Syed Asif S A, Warren O L, Shan Z W, Wu J and Minor A M 2013 Nanomechanical actuation from phase transitions in individual VO₂ microbeams *Appl. Phys. Lett.* **102** 231909
- [112] Lu Y, Ganesan Y and Lou J 2010 A multi-step method for *in situ* mechanical characterization of 1D nanostructures using a novel micromechanical device *Exp. Mech.* **50** 47–54
- [113] Durelli A J, Morse S and Parks V 1962 The theta specimen for determining tensile strength of brittle materials *Mater. Res. Stand.* **2** 114–7
- [114] Gaither M S, DelRio F W, Gates R S and Cook R F 2011 Deformation and fracture of single-crystal silicon theta-like specimens *J. Mater. Res.* **26** 2575–89
- [115] Lu Y, Peng C, Ganesan Y, Huang J Y and Lou J 2011 Quantitative *in situ* TEM tensile testing of an individual nickel nanowire *Nanotechnology* **22** 355702
- [116] Lu Y, Song J, Huang J Y and Lou J 2011 Fracture of sub-20 nm ultrathin gold nanowires *Adv. Funct. Mater.* **21** 3982–9
- [117] Haque M A and Saif M T A 2003 A review of MEMS-based microscale and nanoscale tensile and bending testing *Exp. Mech.* **43** 248–55
- [118] Haque M A and Saif M T A 2002 Application of MEMS force sensors for *in situ* mechanical characterization of nano-scale thin films in SEM and TEM *Sensors Actuators* **97–8** 239–45
- [119] Desai A V and Haque M A 2007 Mechanical properties of ZnO nanowires *Sensors Actuators* **134** 169–76
- [120] Zhang D, Breguet J-M, Clavel R, Sivakov V, Christiansen S and Michler J 2010 *In situ* electron microscopy mechanical testing of silicon nanowires using electrostatically actuated tensile stages *J. Microelectromech. Syst.* **19** 663–74
- [121] Chang T-H and Zhu Y 2013 A microelectromechanical system for thermomechanical testing of nanostructures *Appl. Phys. Lett.* **103** 263114
- [122] Chen L Y, Terrab S, Murphy K F, Sullivan J P, Cheng X and Gianola D S 2014 Temperature controlled tensile testing of individual nanowires *Rev. Sci. Instrum.* **85** 013901
- [123] Kang W and Saif M T A 2011 A novel SiC MEMS apparatus for *in situ* uniaxial testing of micro/nanomaterials at high temperature *J. Micromech. Microeng.* **21** 105017
- [124] Sim G-D, Park J-H, Uchic M D, Shade P A, Lee S-B and Vlassak J J 2013 An apparatus for performing microtensile tests at elevated temperatures inside a scanning electron microscope *Acta Mater.* **61** 7500–10
- [125] Bernal R A, Filleter T, Connell J, Sohn K, Huang J, Lauhon L J and Espinosa H D 2014 *In situ* electron microscopy four-point electromechanical characterization of freestanding metallic and semiconducting nanowires *Small* **10** 725–33
- [126] Kiuchi M, Matsui S and Isono Y 2008 The piezoresistance effect of FIB-deposited carbon nanowires under severe strain *J. Micromech. Microeng.* **18** 065011
- [127] Murphy K F, Piccione B, Zanjani M B, Lukes J R and Gianola D S 2014 Strain- and defect-mediated thermal conductivity in silicon nanowires *Nano Lett.* **14** 3785–92
- [128] Signorello G, Karg S, Björk M T, Gotsmann B and Riel H 2013 Tuning the light emission from GaAs nanowires over 290 meV with uniaxial strain *Nano Lett.* **13** 917–24
- [129] Signorello G, Lörtscher E, Khomyakov P A, Karg S, Dheeraj D L, Gotsmann B, Weman H and Riel H 2014 Inducing a direct-to-pseudodirect bandgap transition in wurtzite GaAs nanowires with uniaxial stress *Nat. Commun.* **5** 3655
- [130] Guan C 2009 *Development of a Closed-loop MEMS Capacitive Force Sensor MS Thesis* (Raleigh, NC: North Carolina State University)
- [131] Filleter T, Ryu S, Kang K, Yin J, Bernal R A, Sohn K, Li S, Huang J, Cai W and Espinosa H D 2012 Nucleation-controlled distributed plasticity in penta-twinned silver nanowires *Small* **8** 2986–93
- [132] Messenger R K, Aten Q T, McLain T W and Howell L L 2009 Piezoresistive feedback control of a MEMS thermal actuator *J. Microelectromech. Syst.* **18** 1267–78
- [133] Brenner S S 1956 Tensile strength of whiskers *J. Appl. Phys.* **27** 1484

- [134] Uchic M D, Dimiduk D M, Florando J N and Nix W D 2004 Sample dimensions influence strength and crystal plasticity *Science* **305** 986–9
- [135] Greer J R, Oliver W C and Nix W D 2005 Size dependence of mechanical properties of gold at the micron scale in the absence of strain gradients *Acta Mater.* **53** 1821–30
- [136] Volkert C A and Lilleodden E T 2006 Size effects in the deformation of sub-micron Au columns *Phil. Mag.* **86** 5567–79
- [137] Shan Z W, Mishra R K, Syed Asif S A, Warren O L and Minor A M 2008 Mechanical annealing and source-limited deformation in submicrometre-diameter Ni crystals *Nat. Mater.* **7** 115–9
- [138] Jennings A T, Li J and Greer J R 2011 Emergence of strain-rate sensitivity in Cu nanopillars: transition from dislocation multiplication to dislocation nucleation *Acta Mater.* **59** 5627–37
- [139] Zheng H, Cao A, Weinberger C R, Huang J, Du K, Wang J, Ma Y, Xia Y and Mao S X 2010 Discrete plasticity in sub-10 nm-sized gold crystals *Nat. Commun.* **1** 144
- [140] Seo J-H *et al* 2011 Superplastic deformation of defect-free Au nanowires via coherent twin propagation *Nano Lett.* **11** 3499–502
- [141] Park H S, Cai W, Espinosa H D and Huang H 2009 Mechanics of crystalline nanowires *MRS Bull.* **34** 178–83
- [142] Magagnosc D J, Ehrbar R, Kumar G, He M R, Schroers J and Gianola D S 2013 Tunable tensile ductility in metallic glasses *Sci. Rep.* **3** 1096
- [143] Bernal R A, Aghaei A, Lee S, Ryu S, Sohn K, Huang J, Cai W and Espinosa H D 2015 Intrinsic Bauschinger effect and recoverable plasticity in penta-twinned silver nanowires tested in tension *Nano Lett.* **15** 139–46
- [144] John C 1975 The brittle-to-ductile transition in pre-cleaved silicon single crystals *Phil. Mag.* **32** 1193–212
- [145] Nakao S, Ando T, Shikida M and Sato K 2006 Mechanical properties of a micron-sized SCS film in a high-temperature environment *J. Micromech. Microeng.* **16** 715–20
- [146] Nakao S, Ando T, Shikida M and Sato K 2008 Effect of temperature on fracture toughness in a single-crystal-silicon film and transition in its fracture mode *J. Micromech. Microeng.* **18** 015026
- [147] Kang K and Cai W 2010 Size and temperature effects on the fracture mechanisms of silicon nanowires: molecular dynamics simulations *Int. J. Plast.* **26** 1387–401
- [148] Kanda Y 1991 Piezoresistance effect of silicon *Sensors Actuators* **28** 83–91
- [149] Rowe A C H 2014 Piezoresistance in Silicon and its nanostructures *J. Mater. Res.* **29** 731–44
- [150] Egerton R F, Li P and Malac M 2004 Radiation damage in the TEM and SEM *Micron* **35** 399–409
- [151] Zheng K, Wang C, Cheng Y-Q, Yue Y, Han X, Zhang Z, Shan Z, Mao S X, Ye M, Yin Y and Ma E 2010 Electron-beam assisted superplastic shaping of nanoscale amorphous silica *Nat. Commun.* **1** 24
- [152] Soudi A, Khan E H, Dickinson J T and Gu Y 2009 Observation of unintentionally incorporated nitrogen-related complexes in ZnO and GaN nanowires *Nano Lett.* **9** 1844–9
- [153] Campbell G H, McKeown J T and Santala M K 2014 Time resolved electron microscopy for *in situ* experiments *Appl. Phys. Rev.* **1** 041101
- [154] Kim J S, LaGrange T, Reed B W, Taheri M L, Armstrong M R, King W E, Browning N D and Campbell G H 2008 Imaging of transient structures using nanosecond *in situ* TEM *Science* **321** 1472–5
- [155] Spolenak R, Ludwig W, Buffiere J Y and Michler J 2010 *In situ* elastic strain measurements—diffraction and spectroscopy *MRS Bull.* **35** 368–74
- [156] Yashinski M S and Muhlstein C L 2013 The role of deposited layers in the nonlinear constitutive behavior of Si nanowires *J. Appl. Phys.* **114** 193507
- [157] Chisholm C, Bei H, Lowry M B, Oh J, Asif S A S, Warren O L, Shan Z W, George E P and Minor A M 2012 Dislocation starvation and exhaustion hardening in Mo alloy nanofibers *Acta Mater.* **60** 2258–64
- [158] Peng C, Zhan Y and Lou J 2012 Size-dependent fracture mode transition in copper nanowires *Small* **8** 1889–94
- [159] Ozkan T, Naraghi M and Chasiotis I 2010 Mechanical properties of vapor grown carbon nanofibers *Carbon NY* **48** 239–44
- [160] Locascio M, Peng B, Zapol P, Zhu Y, Li S, Belytschko T and Espinosa H D 2009 Tailoring the load carrying capacity of MWCNTs through inter-shell atomic bridging *Exp. Mech.* **49** 169–82
- [161] Agrawal R, Peng B, Gdoutos E E and Espinosa H D 2008 Elasticity size effects in ZnO nanowires—a combined experimental-computational approach *Nano Lett.* **8** 3668–74
- [162] Bernal R A, Agrawal R, Peng B, Bertness K A, Sanford N A, Davydov A V and Espinosa H D 2011 Effect of growth orientation and diameter on the elasticity of GaN nanowires. A combined *in situ* TEM and atomistic modeling investigation *Nano Lett.* **11** 548–55
- [163] Tsuchiya T, Jomori T, Ura Y, Sugano K and Tabata O 2008 Fabrication of free-standing fullerene nanowire using direct electron beam writing and sacrificial dry etching *IEEE 21st Int. Conf. Micro Electro Mechanical Systems* pp 689–92